water

MDPI

Article

Assessment of Changes in Groundwater Resources Due to Climate Change for the Purpose of Sustainable Water Management in Hungary

János Szanyi [1,2,*], Hawkar Ali Abdulhaq [2,3,*], Róbert Hegyi [2,4], Tamás Gál [2,3], Éva Szabó [2,5], László Lossos [2,6] and Emese Tóth [1,2]

[1] Department of Geology, University of Szeged, 6720 Szeged, Hungary
[2] National Laboratory for Water Science and Water Safety, 6500 Budapest, Hungary; hegyi.robert@ovf.hu (R.H.); gal.tamas.matyas@szte.hu (T.G.); szaboe@fetivizig.hu (É.S.)
[3] Department of Atmospheric and Geospatial Data Sciences, University of Szeged, 6722 Szeged, Hungary
[4] General Directorate of Water Management (OVF), 1253 Budapest, Hungary
[5] Upper-Tisza-Regional Water Directorate (FETIVIZIG), 4400 Nyiregyhaza, Hungary
[6] Trans-Tisza Region Water Directorate (TIVIZIG), 4025 Debrecen, Hungary
* Correspondence: szanyi@iif.u-szeged.hu (J.S.); hawkar.ali.abdulhaq@szte.hu (H.A.A.); Tel.: +36-20-5018566 (J.S.); +36-70-7895714 (H.A.A.)

Abstract

Climate change is increasingly affecting groundwater resources in the Carpathian Basin, while rising temperatures are likely to increase irrigation demand and pressure on aquifers. We assessed climate- and pumping-driven impacts on the Nyírség recharge–discharge system (north-eastern Hungary) by combining shallow groundwater monitoring (1970–2022) with hydroclimate indicators from CHIRPS precipitation and ERA5-Land air temperature and snow depth (1981–2024). Using these datasets, we developed and calibrated a MODFLOW groundwater-flow model for representative wet (2010) and dry (2022) conditions, incorporating permitted abstraction and scenario-based estimates of unregistered pumping. We then ran scenario simulations to evaluate mid-century (2050) conditions and managed aquifer recharge (MAR) options. Precipitation exhibits strong interannual variability, but the region shows marked warming and a pronounced decline in snow storage, implying reduced cold-season buffering and higher evaporative demand. Simulations reproduce the observed post-2010 decline in shallow groundwater, with the largest decreases in higher-elevation recharge areas, whereas increased pumping mainly intensifies localized drawdown near major well fields. Scenario results indicate that climate-driven reductions in recharge dominate basin-scale declines by 2050, while MAR provides primarily local benefits; direct subsurface injection performs best among the tested options. These findings support practical groundwater management by prioritizing measurable and enforceable abstraction (including unregistered withdrawals), demand-side irrigation efficiency and adaptive caps in recharge areas, and targeted subsurface MAR where source water and infrastructure are available.

Keywords: climate change; groundwater level decline; Hungary; numerical modeling; managed aquifer recharge (MAR); illegal wells; groundwater governance; decision support; digital twin

Academic Editors: Liang Yuan and Thomas Ramsey

Received: 26 January 2026
Revised: 25 February 2026
Accepted: 25 February 2026
Published: 19 March 2026

1. Introduction

Access to water is crucial for human survival and prosperity, forming the basis of well-being and economic development [1–3]. However, there are many signs that climate change is shifting the water cycle towards increased seasonal variability. This results in a more erratic and uncertain supply of both surface water and groundwater [4–7].

Hydrometeorological trends are changing at a faster rate in the Carpathian Basin, especially in the Great Hungarian Plain, than the global average. The rate of warming is accelerating, and the reconfiguration of major wind systems in the atmosphere is becoming more evident [8]. These changes result in shifts in the spatial and temporal distribution of precipitation, a decline in snowfall and river flow, and variations in the maximum annual water levels of rivers, leading to a general decrease in groundwater levels, particularly in areas of recharge. Due to climatic conditions, particularly the increasingly frequent periods of drought in recent years, it is not possible to cultivate corn, sunflowers, rapeseed, tobacco and horseradish efficiently without irrigation. Reported irrigation covers ~17,000 ha, whereas ~100,000 ha may be irrigable. Together with authority inspections, this implies that undeclared irrigation withdrawals are substantial. The volume not included in declarations is estimated at 35–70 million m^3/year (best estimate ~50 million m^3/year) [9]. Declining groundwater levels have led to an increase in both legal and illegal water extraction, which has further exacerbated the situation. These effects can be reduced by using managed aquifer recharge technologies (MAR). This involves storing water—such as surface water, stormwater or treated wastewater—in aquifers using infiltration basins, streambeds, recharge wells or riverbank filtration, for example. MAR can improve water security and groundwater quality through subsurface filtration. It is a widely used sustainable water management strategy, particularly in regions where water is scarce [10,11]. A special method of recharging the aquifer involves using wells to inject water through drainage pipes [11,12]. This allows larger quantities of water to be pumped in without causing a significant rise in the water level at a particular location.

International studies show that climate change affects groundwater not only through changes in annual precipitation, but also through shifts in seasonality and storm intensity, snow accumulation and melt, and atmospheric evaporative demand. Together, these factors control groundwater recharge and the persistence of drought impacts [13–15]. These processes commonly lead to the strongest groundwater-level declines in recharge-dominated areas, and they complicate attribution because observed changes may reflect the combined influence of climate variability, land use, and groundwater abstraction [13,16].

To quantify these coupled drivers, many recent studies combine long-term groundwater monitoring with hydroclimate indicators derived from remote sensing and reanalysis products and use physically based groundwater-flow models (often MODFLOW-based) to test scenarios and support management decisions [17–19]. Such model frameworks are increasingly used to separate climate-driven and pumping-driven components of groundwater decline, and to evaluate adaptation options such as managed aquifer recharge (MAR), changes in irrigation demand, and governance measures that improve compliance and monitoring [14,16,20,21]. However, results are often sensitive to assumptions about recharge, evapotranspiration, and poorly observed withdrawals, underscoring the importance of transparent scenario design and explicit treatment of unregistered abstraction where it is relevant [22–24]. These international findings are highly relevant for temperate, lowland recharge systems such as those of the Carpathian Basin, where groundwater supports irrigation and groundwater-dependent ecosystems. However, integrated assessments in Central–Eastern Europe that jointly (i) link observed hydroclimatic shifts to recharge change, (ii) separate climate effects from permitted and unregistered abstraction, and

(iii) evaluate managed aquifer recharge (MAR) as an adaptation option using a calibrated groundwater-flow model remain limited.

In this context, the novelty of this study is threefold. First, we integrate multi-decadal groundwater monitoring with remote-sensing/reanalysis hydroclimate indicators in a single, reproducible workflow to characterize observed hydroclimatic change and groundwater response in a temperate lowland recharge system. Second, we explicitly incorporate both permitted abstraction and scenario-based estimates of unregistered (illegal) pumping into the numerical groundwater-flow model, allowing a transparent assessment of how uncertain withdrawals may amplify climate-driven declines. Third, we use the calibrated model to test management-relevant scenarios to mid-century (2050), including managed aquifer recharge (MAR) options, and we frame the modelling workflow as a practical step toward an updatable decision-support "digital twin" that can be refined as new monitoring and abstraction data become available.

Accordingly, this paper aims to: (i) quantify observed groundwater-level and hydroclimatic trends; (ii) calibrate a groundwater-flow model under contrasting wet and dry conditions to separate climate-driven and pumping-driven effects; and (iii) evaluate scenario-based changes by 2050, including MAR options, to support sustainable groundwater management. We apply the framework to the Nyírség region in north-eastern Hungary; the study area is described in Section Study Area.

This study analyses the role of natural and anthropogenic impacts in an attempt to predict changes in the groundwater level by 2050. The two most extreme weather periods of the 21st century were in 2010, when 896 mm of precipitation fell, one and a half times the average of 585 mm, and in 2022, which was the hottest and driest year, with only 450 mm of precipitation. We compared our forecasts to those years [25]. We use numerical simulation to make this prediction and also offer recommendations for mitigating the expected negative impacts. To this end, we focus on a specific sample area: the Nyírség region. The Nyírség region is located in the north–east of the Hungarian Great Plain. It is the region's highest landscape unit, rising like an island above the surrounding terrain, with an area of 5100 km^2 (Figure 1). It has an average altitude of 140 m above sea level, with the central part exceeding 180 m and the edges averaging 100–110 m.

The depth and annual changes in shallow groundwater are influenced by the flow regime, since the recharge areas are replenished directly by precipitation, with no subsurface inflow [26,27]. The Nyírség is unique in that it is a hydraulically uniform water body, with recharge and discharge areas that belong to it. Areas above 125–130 m are recharge areas, while those below this level are characterised as flow-through or discharge areas [28,29]. This makes the region an ideal demonstration area for the combined effects of climate change and human activity on the water balance [30].

Over the past two decades, numerous studies have addressed the spatial analysis of groundwater level changes in the Great Plain [31,32]. One of the main approaches to these analyses is the spatial assessment of changes based on 'groundwater change maps'. In this process, changes in the groundwater level are compared to those in a selected reference period, and the difference is depicted on a map using geoinformatics and geostatistical methods. Compared to the 1961–1965 reference period, the effects of rainy and dry periods are most pronounced in the Hátság region, between the Danube and Tisza rivers (the Danube–Tisza Interfluve) and in the Nyírség region. These areas can be considered as recharge areas. The extent of the changes was assessed based on altitude above sea level. In the Danube-Tisza Interfluve region, a significant disparity in water scarcity has emerged between areas above and below 120 m since the mid-1980s. The higher regions have experienced more pronounced scarcity (Figure 2), a phenomenon that emerged a few years later in the Nyírség region [31]. However, in recent years, the rate

of decline in the water level has accelerated, leading to a deterioration in both ecological values and agricultural production. The fact that recharge areas are fed exclusively by precipitation [33,34] clearly indicates a change in climatic conditions.

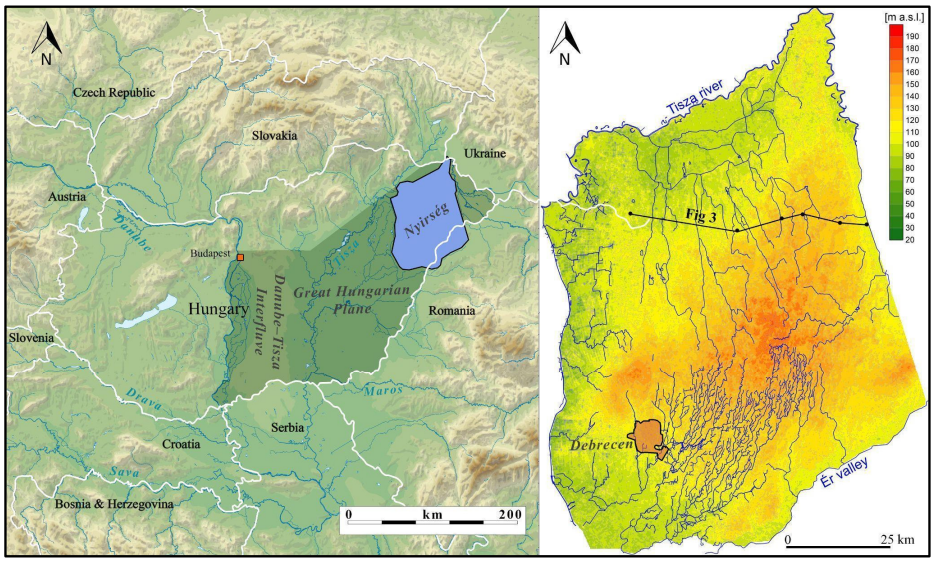

Figure 1. Topography of the Pannonian Basin, with highlights of the Nyírség region and the location of the cross-section in Figure 3.

The rest of the paper is organized as follows: Section 2 is the Study Area and Data, Section 3 discusses the Methodology, Section 4 provides the results, Section 5 is the Discussion and Section 6 concludes.

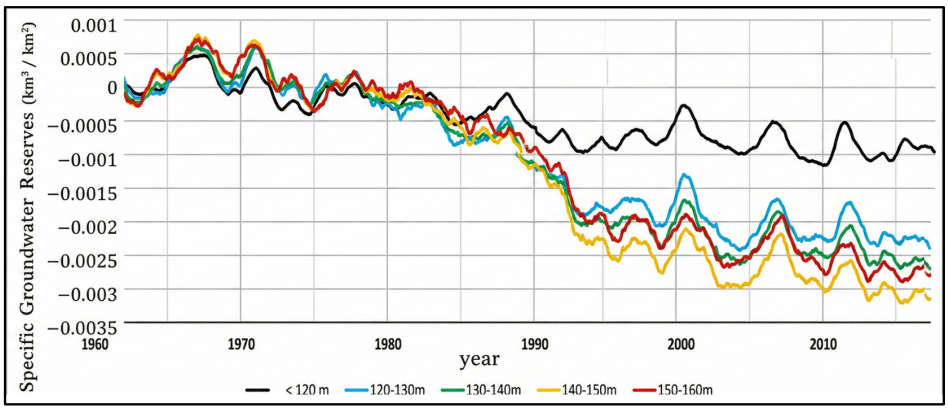

Figure 2. Changes in specific groundwater reserves in the Danube-Tisza Interfluves, categorised by elevation (1960–2017), with a reference period of 1961–1965. From [31] modified.

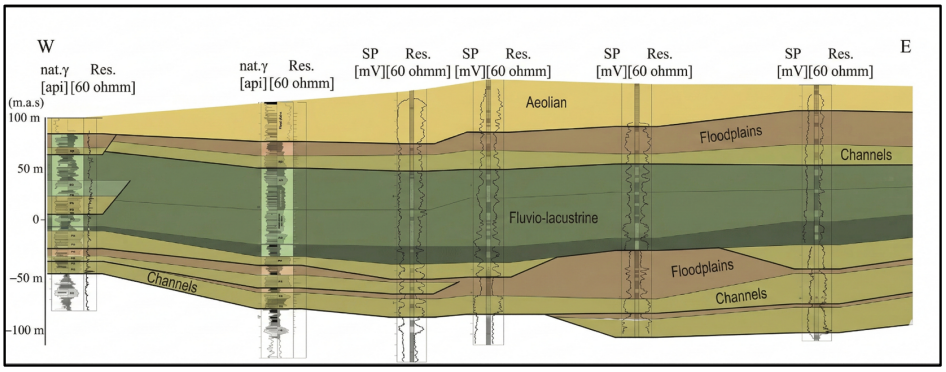

Figure 3. West–East sedimentological section of Nyírség (section position see Figure 1) [35] modified.

2. Case Study

Study Area

In terms of structural geology, the eastern and western boundaries of the Nyírség region are well defined, following north–south tectonic lines, while it is bordered by the Tisza River to the north and the Ér Valley to the southeast [35–37].

The Nyírség geological formations are characterised by thick layers of Tertiary volcanic rocks, which were deposited on top of a crystalline basement that is not well understood. These volcanic rocks were followed by sediments from the Late Miocene Pannonian Lake, which are between 1000 and 1200 m thick. During the Pleistocene, the area was uplifted, causing the upper 100–200 m of the Upper Pannonian formations filling the basin to erode. This was followed by a Quaternary series with an average thickness of 200 m, which was deposited discordantly [38,39]. The thickness of the sediments deposited during the Holocene is less than one metre.

The region was essentially shaped by the surface-forming activity of river water and wind during the Neogene development. The stratigraphic interpretation of the Quaternary fluvial succession was developed in the last decade [40–42]. The sedimentation changed from deltaic into alluvial facies associations [35,43–45]. The river sediment is thickest along the axis of the Nyírség. All the rivers in the north-eastern part of the Great Plain contributed to the formation of the 120–300-metre-thick layer sequence, the most significant of which were the Tisza and the Szamos [28,35,43]. Some of the river sand turned into aeolian sand, covering large areas to a depth of over 30 m in places. The gravel, sand and floodplain clay sediments in the deeper basins are arranged in a rhythmic pattern, reflecting the periods of subsidence and the climatic cycles that influence erosion and deposition. The Tertiary hills located between the sub-basins were covered only by drifting sand, falling dust and fine sand or silt from major floods [44–47] (Figure 3).

The Pannonian Basin is one of the world's 70 largest aquifer systems [48]. From a hydrodynamic perspective, the Hungarian Great Plain can be divided into two flow systems: a shallower one and a deeper one. The upper system extends from Quaternary to Late Miocene formations, which are highly permeable and porous. This forms an extensive gravitational flow system [27,28]. Meanwhile, a significant overpressure flow system has developed below, primarily due to regional compression and the clay formations of Lake Pannon in the upper sequence [48,49]. This paper focuses on the unconfined, gravitational flow system. The shallow groundwater level follows the contours of the terrain (Figure 4). The Quaternary sediments of the Nyírség region are part of a large, single, leaking aquifer system [28,29], where recharge depends on precipitation infiltrating the surface at higher elevations in the centre. Significant differences exist in the pressure levels of the Upper, Middle and Lower Pleistocene layers [28,29]. In the central areas of Nyírség, for instance, under natural conditions, the difference in piezometric levels of water stored in the Upper and Lower Pleistocene layers was 30–35 m. This meant that the water level in wells screening the Lower Pleistocene was that much deeper (Figure 5). However, the natural flow system was altered somewhat by the production of water from wells, which began in the mid-19th century and accelerated at the beginning of the 20th century, particularly in the surroundings of the bigger cities [28,29,44].

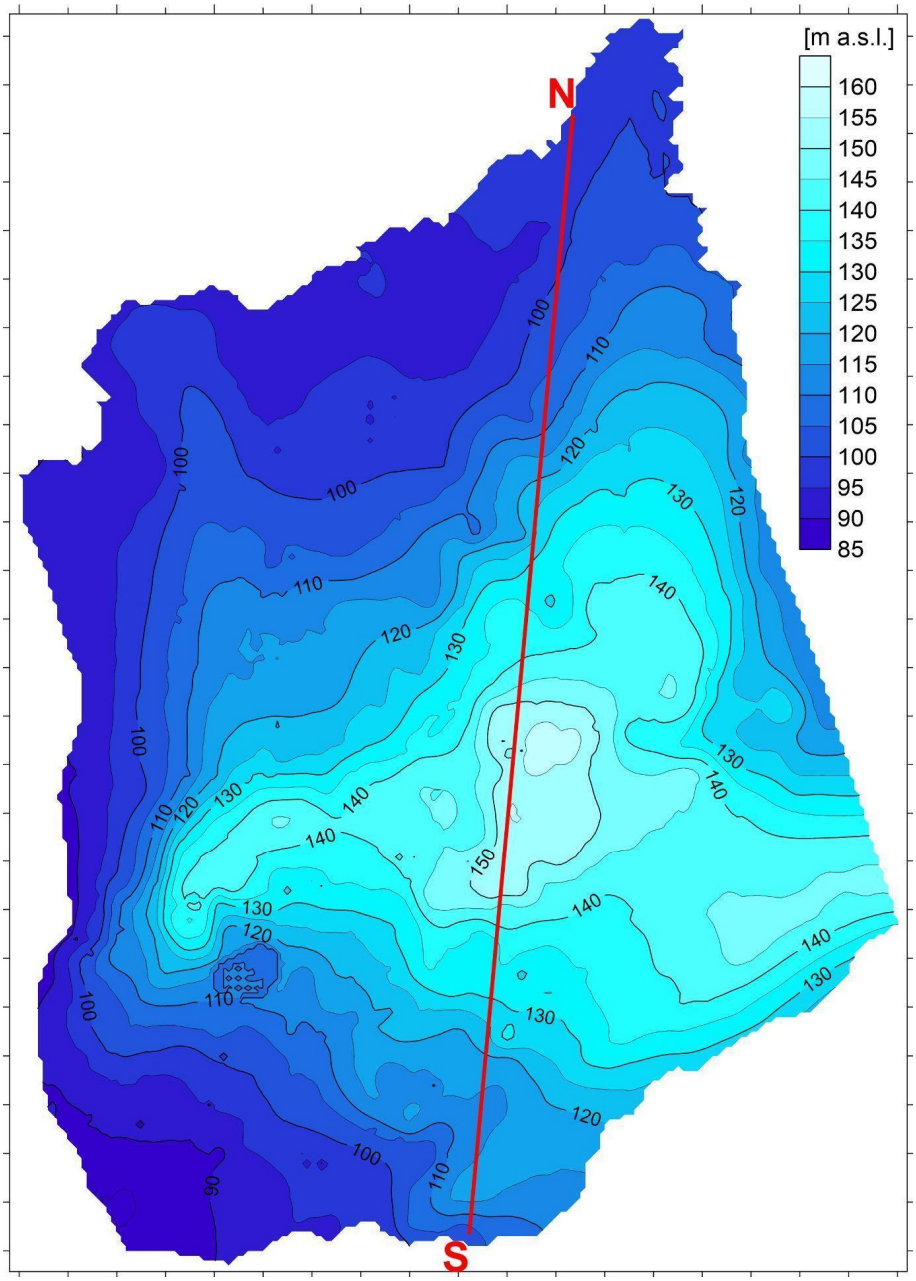

Figure 4. Shallow groundwater level in Nyírség area (m a.s.l.). The red line indicates the trace of the south–north hydrogeological cross-section shown in Figure 5.

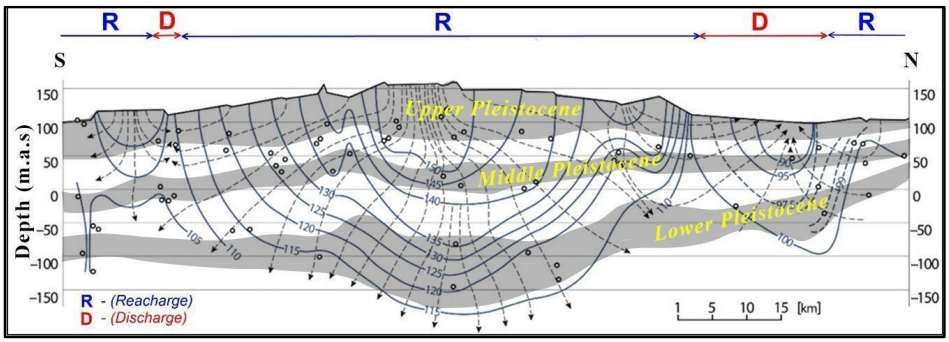

Figure 5. The south–north groundwater flow system profile of the Pleistocene formations of the Nyírség, showing the location of the wells used (circles), and indicating the flow regime [28] modified.

3. Methodology

3.1. Hydrogeological Data

We compiled data on wells from the Water Management Authorities and the National Water Management Directorate, creating a comprehensive database. We checked the data for completeness and corrected the coordinates and data for any wells with errors. In the new database, we have deleted wells that had no production data or had already been abandoned. The resulting database contains a total of 3141 wells. From this large dataset, we selected wells with filters located below 50 m to create a separate database for shallow groundwater wells. Of these, 1353 have filters located deeper than 50 m, while 1788 are shallower than 50 m. Next, we examined water production. We removed wells with completely inaccurate or missing production data. Between 1978 and 2022, a total of 2377 wells in the area had time series data. The Water Authorities hold information on the production of illegal wells, which exceeds the total production of legal wells. The methodology subchapter explains how these are taken into account.

Water levels in watercourses and reservoirs (mostly lakes) in the modelling area are documented on a monthly basis. The time period covered by the data series varies greatly, with time series of over 100 years available for major rivers and data for canals available from the 1980s onwards.

The data required for numerical simulation was previously derived from work carried out in the field [37,50].

3.2. Hydroclimate Data Sources

The hydroclimate views implemented in the application are based on a consistent set of datasets accessed through Google Earth Engine and on derived statistics computed in Python v3.14 [51]. As summarised in Table 1, daily precipitation is obtained from the CHIRPS product, while ERA5-Land provides hourly fields of snow depth, 2 m air temperature and 2 m dewpoint temperature, from which annual means and five-year running averages are calculated. Spatial products, including GeoJSON point samples and interpolated maps, are generated from five-year ERA5-Land composites sampled over the buffered area of interest (AOI) [52]. All datasets are accessed through the Google Earth Engine Code Editor or Python application programming interface (API) and subsequently processed and visualised in a Python-based CodeStudio environment. The cached AOI-mean daily precipitation time series and the five-year GeoJSON samples constitute reproducible intermediate artefacts that will be distributed alongside the accompanying code repository [53].

For the illegal-well case study in the Nyírség region, normalized difference vegetation index (NDVI) and land surface temperature (LST) were derived from Landsat 8 Collection 2 Level-2 Tier 2 imagery acquired between 10 and 26 July 2022 through Google Earth Engine. NDVI was calculated from the near-infrared (Band 5) and red (Band 4) bands, while LST was obtained from thermal Band 10, and both raster products were clipped to the study area. An irrigated-field shapefile was used to delineate agricultural land and to define cropland polygons and their centroids as initial candidate locations for wells. In addition, a point dataset of existing wells, stored in the national Hungarian local coordinate system (Egységes Országos Vetület—EOV), together with land-cover shapefiles representing forests, water bodies and wetlands, was used to construct buffered exclusion zones. All auxiliary datasets were processed in Python within the same CodeStudio environment as the hydroclimate analysis. Data not directly available through Google Earth Engine, including the irrigated-field shapefile, real-well point layer and land-cover shapefiles, will be released alongside the Earth Engine scripts and Python notebooks in a public repository, subject to the licensing terms of the original data providers.

Table 1. Overview of primary datasets and processing steps underlying each hydroclimate dashboard view.

View	Primary Dataset(s)	Processing Summary	Notes
Daily Precipitation Trends	CHIRPS daily precipitation (UCSB-CHG/CHIRPS/DAILY)	cached_daily_stats pulls daily AOI means; user-selected date range and rolling window generate raw vs. smoothed series	Requires analysis_geom AOI and optional shapefile overlay for context
Annual Intensity Band Totals	CHIRPS daily precipitation	Day-level precipitation split into <10 mm, 10–30 mm, >30 mm bins before annual sums	Years reindexed to maintain continuity even if some bins are empty
Annual Heavy Rain vs. Total with Snow & Temperature	CHIRPS daily precipitation; ERA5-Land hourly snow depth (snow_depth) and 2 m temperature (temperature_2m)	Annual totals and heavy-day contributions from CHIRPS merged with ERA5 annual snow/temperature averages (Celsius conversion)	Snow/temperature lines scaled by constants for visualization; heavy threshold adjustable in sidebar
5-Year Averages: Snow & Temperature	ERA5-Land hourly snow depth & temperature	Annual ERA5 snow & temperature means smoothed via 5-year moving averages	Chart uses independent y-axes with color-matched labels
5-Year Averages: Snow, Temperature & Humidity	ERA5-Land hourly snow depth, 2 m temperature, and dewpoint (dewpoint_temperature_2m)	Same as snow/temp above plus relative humidity (RH) derived from temperature & dewpoint using Magnus relation, then 5-year MA	Humidity clipped to 0–100% before smoothing; axes use distinct colors (snow blue, temp red, humidity pale blue)
5-Year Averages: Snow & Precipitation	ERA5-Land snow depth; CHIRPS precipitation totals	Annual snow means (ERA5) and precipitation sums (CHIRPS) converted to 5-year moving averages	Highlights relative long-term trends between cryosphere and moisture supply
Saved 5-Year GeoJSON Maps	ERA5-Land five-year composites for snow depth & temperature	ERA5 hourly stacks averaged over trailing 5-year windows, sampled (~4k points, 10 km scale, buffered AOI) and exported as GeoJSON	GeoJSONs stored in mapdata/; zip bundle created for download
Interpolated 5-Year Maps	GeoJSON samples produced from ERA5-Land composites	GeoJSON lon/lat/value points interpolated onto grids via radial basis function RBF fallback to inverse-distance weighting (IDW), masked to AOI, and rendered/compared	Supports difference/magnitude plots between latest and earliest windows

3.3. Groundwater Flow Simulation and Model Calibration

We used the Processing MODFLOW Pro v8 environment for our hydrodynamic calculations. This software is one of the MODFLOW clones and has extensive calibration references. It supports more MODFLOW packages than other clones and can easily be linked to Surfer, the Windows-based software for map editing and spatial modelling [18,26,54]. In the MODFLOW model, trial-and-error calibration is an iterative, manual process in which the model parameters are adjusted until the calculated results adequately fit the measured data, i.e., until the RMSE error becomes sufficiently small. The model was calibrated using data from two selected years: the wet year of 2010 and the dry year of 2022, for which 120 monitoring well data were used (Figure 6). During calibration, we adjusted the values for the hydraulic conductivity, infiltration from precipitation and evapotranspiration, as well as the extent of illegal water withdrawal. The estimated yield of illegal wells is 30–70 million cubic metres per year. Calibration produced a best-fit estimate of unregistered pumping of 58 million m^3/year (±20%), consistent with estimates provided by the water authorities [9]. Furthermore, as the water level in the wells near the Tisza River in

the eastern part of the model was higher than the measured value during the simulation, we increased the conductance of the Tisza riverbed sediment tenfold (i.e., we increased the riverbed hydraulic conductivity). This is also likely due to the presumed incision of the riverbed.

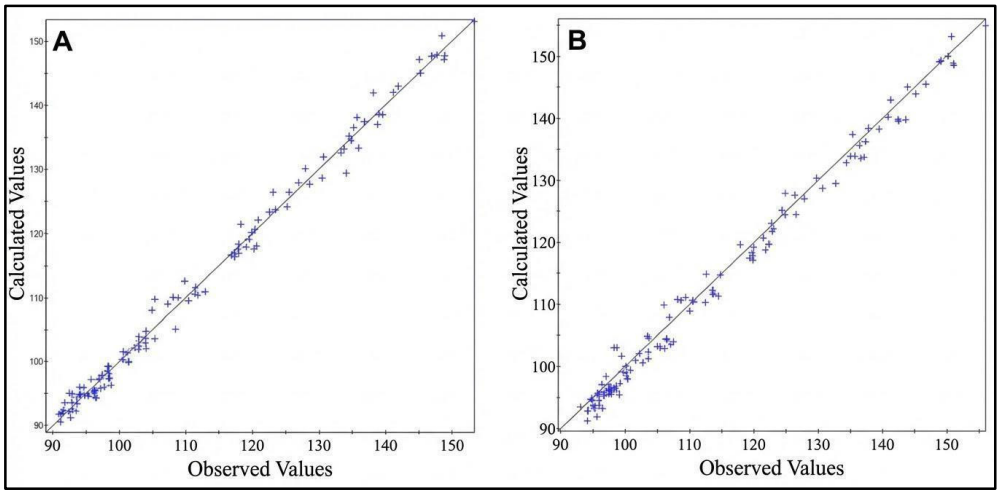

Figure 6. Correlation and variance between observed and calculated water levels in monitoring wells following calibration (**A**) during the dry season, (**B**) during the wet season.

The final calibration results were 1.52 m RMSE for the dry model and 1.99 m RMSE for the wet model. The correlation between the measured and calculated values was 0.996 in both cases. These values were deemed acceptable as there was no observed systematic bias and subsequent calibration iterations did not result in any significant improvement in the RMSE.

While the iterative and non-linear nature of the model makes it impossible to quantify model uncertainty directly, sensitivity testing shows which parameters are most important and allows us to understand how the model responds to changes. The sensitivity of the model to individual input parameters was assessed by comparing the effects on shallow aquifer water levels of different model runs. The infiltration and evapotranspiration values were first increased by 20%, then by 50%, and then decreased by these amounts. When we also altered the spatial distribution of these parameters, the model became unstable and RMSE increased by at least one order of magnitude. The results showed that the model was more sensitive to infiltration, particularly in higher-elevation areas or areas of greater topographic relief. Meanwhile, the evapotranspiration value had less of an effect on the model. When infiltration was lower and evaporation was higher, groundwater levels hardly changed (the RMSE value increased by a factor of 1.5), as not much more water could evaporate due to the decrease in groundwater levels, even with higher evapotranspiration. We examined the effect of the hydraulic conductivity separately. The distribution of this parameter has been examined in several previous models, and we refined their values by taking soil types into account. Increasing this value fivefold increased the range of influence of the channels (the zone showing a water level rise of at least 5 cm) from 180–300 m to 600–1000 m, whereas reducing it to one-fifth resulted in almost no detectable effect.

3.4. Pre-Processing Hydroclimate Data

Daily precipitation data were derived from the CHIRPS global precipitation dataset (Google Earth Engine collection UCSB-CHG/CHIRPS/DAILY). For each day within the study period, precipitation fields were clipped to the analysis geometry and spatially averaged to obtain an AOI-mean daily precipitation time series expressed in millimetres per day; the resulting series was stored as a time-indexed dataframe and cached to ensure consistent

reuse across all subsequent analyses and visualizations [55]. Land surface variables were obtained from the ERA5-Land reanalysis as hourly fields accessed through Google Earth Engine, including snow depth, 2 m air temperature and 2 m dewpoint temperature. These hourly variables were clipped to the analysis geometry and aggregated to calendar-year means, with temperature variables converted from Kelvin to degrees Celsius. Unless stated otherwise, all annual statistics were computed for complete calendar years within the user-defined analysis period (data_year_min to data_year_max). A schematic overview of the complete hydrodynamic data workflow and processing steps is provided in Figure 7.

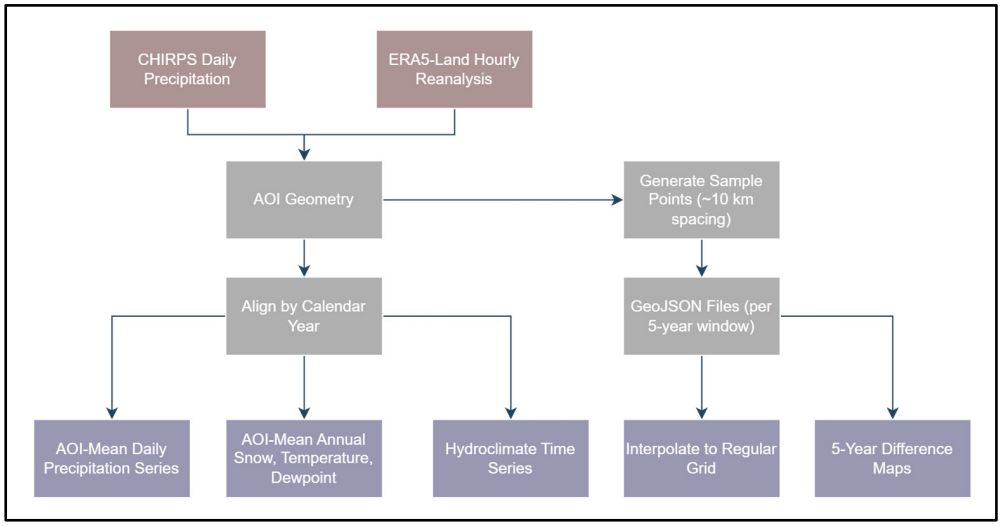

Figure 7. Schematic overview of the hydroclimate workflow, in which CHIRPS daily precipitation and ERA5-Land hourly variables are clipped to the area of interest and processed in parallel to produce AOI-mean time series and multi-year spatial composites for consistent hydroclimate analysis.

Spatial patterns were examined by aggregating ERA5-Land snow depth and 2 m air temperature into non-overlapping five-year composites. The full analysis period was partitioned into consecutive five-year windows (e.g., 1981–1985 to 2020–2024), within which all hourly ERA5-Land images were averaged to produce mean snow depth and temperature rasters that were subsequently clipped to the buffered analysis geometry. To facilitate data transfer and downstream analysis, each five-year composite was reduced to point samples by generating approximately 4000 pseudo-random locations within the buffered area of interest using a pixelLonLat-based sampling scheme at a nominal spacing of ~10 km; snow depth and temperature values were extracted at these locations, optionally clipped to a shapefile-defined AOI, and exported as GeoJSON files that were bundled for distribution and previewed as scatter maps over the AOI outline. Gridded surfaces were then reconstructed from the GeoJSON samples in Python by interpolating the point values onto a regular grid using radial basis function interpolation, with inverse-distance weighting applied as a fallback when necessary; the resulting grids were masked to the AOI polygon, visualised with standard plotting tools, and differenced between successive five-year windows to quantify the spatial magnitude and direction of change in both snow depth and air temperature.

3.5. Temporal Hydroclimate Indicators Calculator Methods

Daily precipitation trends were examined by filtering the cached CHIRPS time series to a user-defined date range and applying a moving-window mean with a selectable length between 1 and 60 days to the AOI-mean precipitation series, producing paired series of raw daily precipitation and smoothed values that facilitate interpretation of individual rainfall events and their temporal persistence [56–58]. To assess the contribution

of different rainfall intensities to annual totals, each daily precipitation value was classified into three intensity categories (<10 mm day^{-1}, 10–30 mm day^{-1}, and >30 mm day^{-1}), and for each calendar year the daily amounts within each category were summed to obtain annual accumulations and their relative contributions to total precipitation [59–61]. We evaluated the relationship between heavy rainfall, annual precipitation, snow depth, and air temperature by combining CHIRPS and ERA5-Land data. Annual precipitation totals were calculated by summing daily CHIRPS values, and the heavy-rain component was defined as cumulative precipitation on days exceeding a user-defined threshold (25 mm by default). Annual mean snow depth and 2 m air temperature were derived from ERA5-Land and scaled (for plotting only) to enable joint visualization with precipitation using separate axes.

Multi-year variability was assessed using trailing five-year moving averages derived from ERA5-Land data. Annual mean snow depth and 2 m air temperature were first calculated for each calendar year and subsequently smoothed using a trailing five-year window, with the initial years incorporating all available preceding data. These smoothed series were displayed together using independent vertical axes to emphasise long-term trends in cryospheric and thermal conditions while preserving interannual variability [56,57,62]. Relative humidity was estimated by combining ERA5-Land 2 m air temperature (T) and dewpoint temperature (Td), both converted to degrees Celsius, using a Magnus-type formulation, after which RH values were constrained to the physical range of 0–100%, aggregated to annual means, and converted to trailing five-year averages for joint visualization with snow depth and air temperature using separate, colour-matched axes [63,64].

$$RH = 100 \times exp\left(\frac{(17.625\ Td)}{(Td + 243.04)} - \frac{(17.625\ T)}{(T + 243.04)}\right)$$

3.6. Identification of Potential Illegal Wells in the Nyírség Region

The location of illegal wells and the determination of yields are based on assumptions. These assumptions are primarily derived from satellite information. The irrigated-field dataset used in this study is based on a polygon provided by the national water authority delineating officially registered irrigated parcels, which was stored and processed as a standard shapefile and served as the basis for all subsequent analyses (Figure 8). The shapefile was first cleaned by merging neighbouring fields using a configurable buffer distance, with before–after geometries examined to verify the integrity of the consolidated field boundaries. The resulting field polygons were then used to generate virtual well locations by placing points randomly around polygon centroids, with parameters controlling the offset range and the number of wells assigned to different field-size classes. These candidate wells were subsequently filtered to remove points located too close to one another or to existing real wells, ensuring appropriate spatial separation and compliance with minimum-distance criteria, and the intermediate results were visually inspected on filtered maps. The final dataset, comprising real wells and the retained virtual wells, was presented as an interactive map that can be exported as an HTML file. To ensure full reproducibility and accessibility, the complete workflow was implemented as an open Streamlit and GitHub v1.0 project and is publicly available at Abdulhaq, 2025 [65], allowing users to reproduce all cleaning, generation, filtering and visualization steps end-to-end.

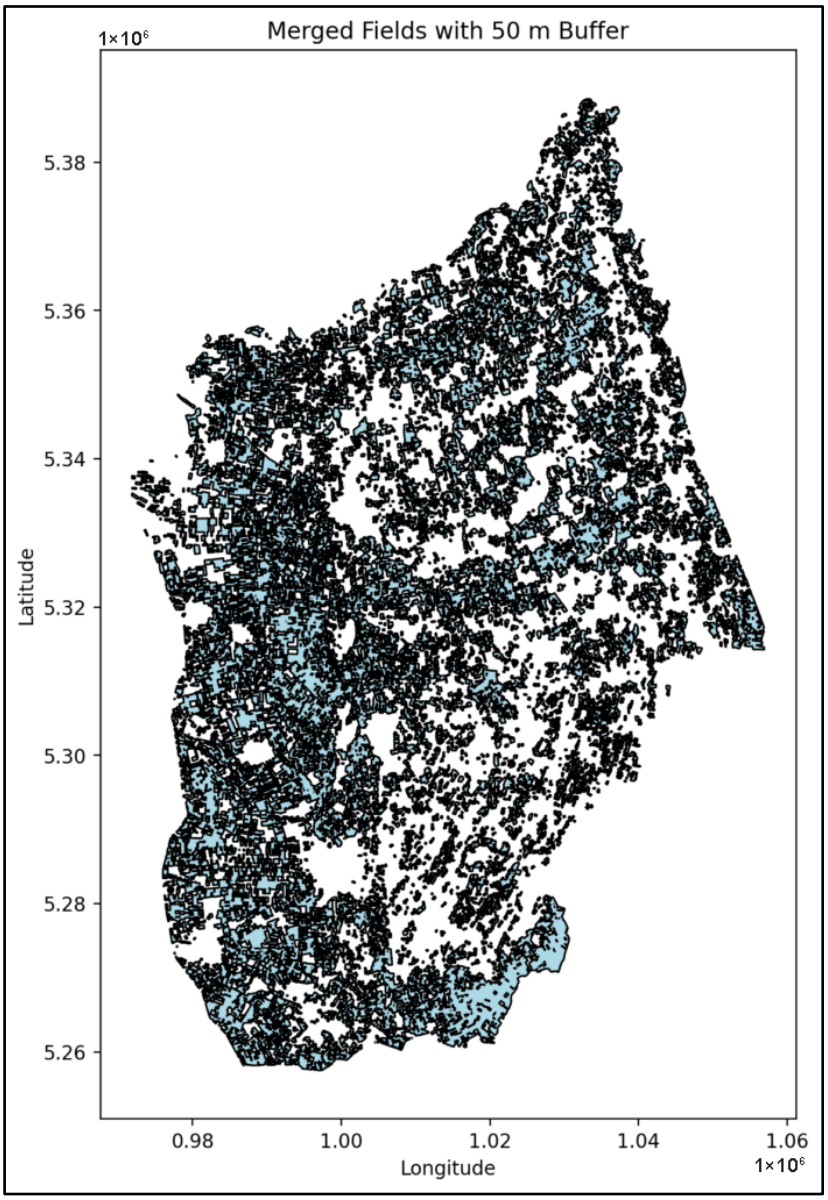

Figure 8. Irrigated fields after merging neighbouring parcels using a 50 m buffer, forming consolidated field polygons used as the basis for subsequent analyses.

3.7. Software Environment, Reproducibility and Use of Generative AI

All analyses were conducted for a user-defined area of interest (AOI) using a reproducible workflow that couples Google Earth Engine (GEE) with Python-based post-processing (Figure 9). The AOI was specified either as a GEE asset (AOI_ASSET_ID) or via an uploaded shapefile; when both were available, the shapefile geometry was used to define the effective analysis region (analysis_geom) [66,67]. For steps requiring spatial sampling beyond the nominal AOI (e.g., interpolation of gridded surfaces), analysis_geom was expanded by a fixed buffer distance (SAMPLE_BUFFER_METERS) to reduce edge effects. Most data acquisition, spatial aggregation, and other computationally intensive operations were executed in GEE using the JavaScript Code Editor and the Earth Engine Python API, whereas downstream processing, spatial analysis, and visualization were carried out in Python (v3.x) within a CodeStudio development environment [51,67,68]. Python post-processing included cleaning sampled datasets, generating and filtering candidate wells, interpolating five-year spatial products, and producing static and interactive visualizations using standard scientific and geospatial libraries [51,67,68]. The CHIRPS daily precipita-

tion, ERA5-Land reanalysis, and Landsat 8 Level-2 datasets used in this study are publicly available through GEE, and all derived products (including AOI-wide hydroclimate time series, five-year GeoJSON samples, interpolated grids, and the Categorized_temp.xyz candidate-well dataset), together with the Earth Engine scripts and Python notebooks, will be made available in a public repository upon publication with no anticipated restrictions on access. Generative AI tools were used in a limited and transparent manner: GitHub Copilot (formerly Codex Copilot v5.1) assisted with routine code development, and a large language model supported refinement of the Materials and Methods text; all AI-assisted outputs were reviewed and revised by the author, who retains full responsibility for the scientific content and interpretation [69–72]. This approach is consistent with the authors' broader use of reproducible, Python-based subsurface analytics in other Hungarian case studies [73,74].

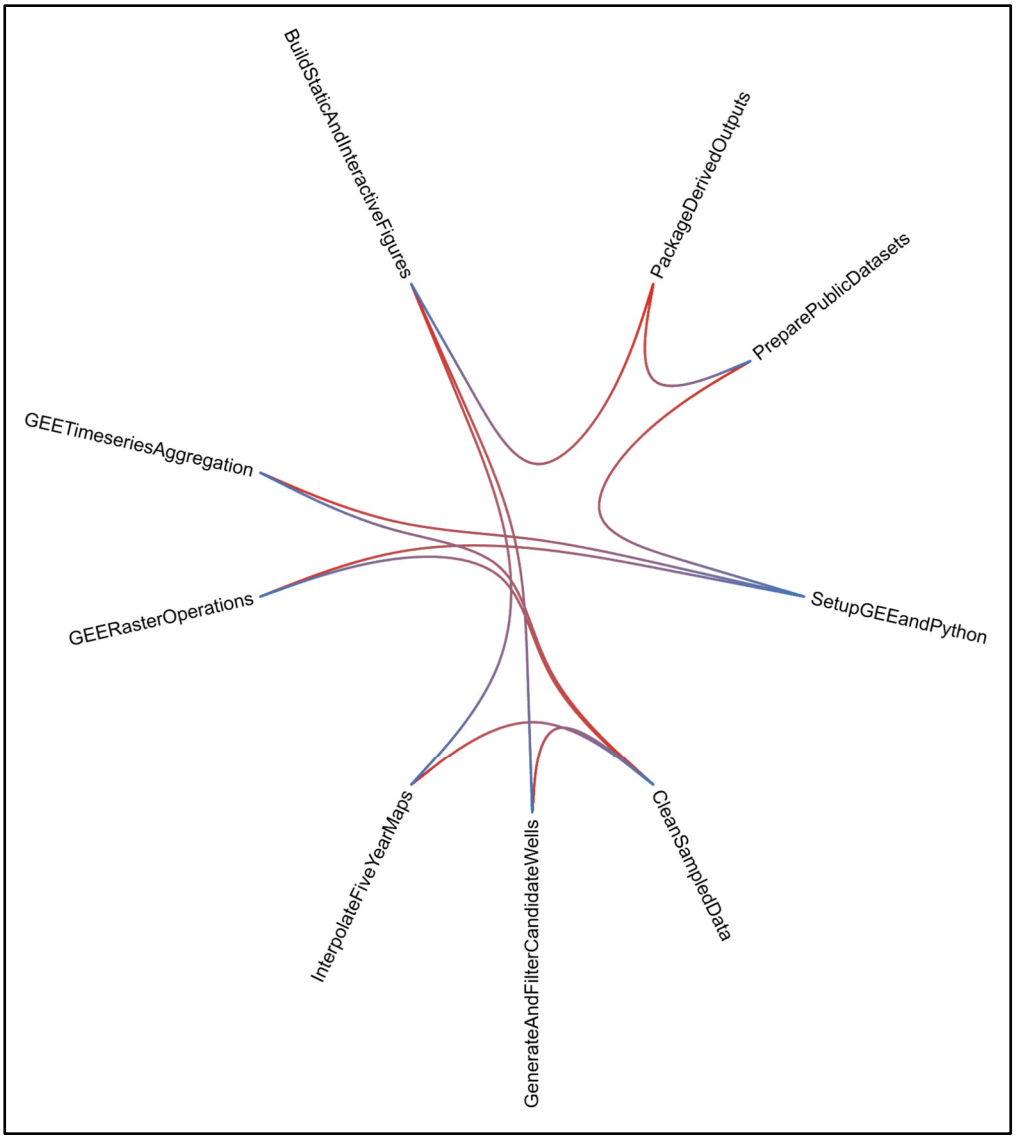

Figure 9. Radial flow chart (Blue to Red direction) illustrating the integrated GEE–Python workflow, from AOI definition and buffered spatial sampling to cloud-based processing in Google Earth Engine and subsequent analysis and visualization in Python.

4. Results

4.1. Groundwater Level Changes

To investigate changes in the groundwater level in the Nyírség region, we analysed more than 50 years' worth of time series data (1970–2022) from 48 shallow groundwater monitoring wells. We plotted the water level time series of the wells against elevation above sea level in 10 m increments, covering ranges of 100–160 m. After 2010, it can be observed that there has been no significant decrease in areas below approximately 130 m a.s.l. (Figure 10); the trend in water level decline is similar to that between 1980 and 1995, except for a few wells. In monitoring wells located near large cities, the water level has remained virtually unchanged over the past 50 years, indicating continuous groundwater recharge from leaks in the water supply network. In contrast, in areas above 130 m, most wells experienced a continuous and significant drop in water levels of up to 3 m after 2010. These areas are clear inflow areas that react most quickly to a decrease in the amount of water replenished by infiltration (Figure 11).

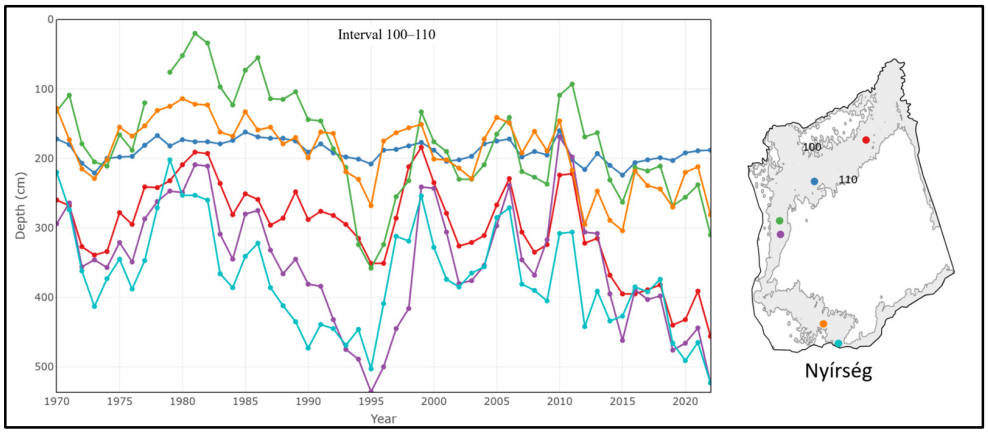

Figure 10. Time-series of groundwater level data located between 100 and 110 m above sea level between 1970 and 2022, with the location of the wells indicated.

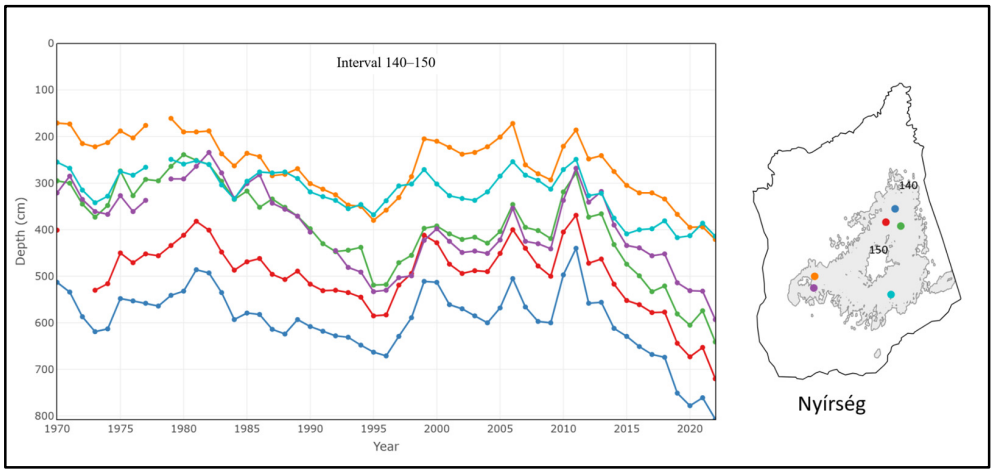

Figure 11. Time-series of groundwater level data located between 140 and 150 m above sea level between 1970 and 2022, with the location of the wells indicated.

From the summer data series consisting of monthly minimum and maximum water levels, we selected June 2010 as the wettest period and September 2022 as the driest [75,76], in order to prepare a map of high and low groundwater levels for the entire Nyírség region, based on data from monitoring wells [75–77]. First, we transformed the groundwater levels measured in the wells into a normal distribution using logarithmic transformation [77].

Then, we performed interpolation at the grid nodes using kriging with a composite semivariogram. We then converted these values back to obtain the calculated groundwater level values at the grid points, which we plotted on a map of the Hungarian part of the Nyírség region (Figures 12 and 13). Based on these figures, the groundwater is at a significant depth of 7 m, even during the wet period. During the dry period, it is deeper than 10 m in the highest part of the Nyírség region [78,79]. At the same time, the groundwater is similarly deep in the north-eastern part of the area despite this being a discharge area along the Tisza River. This is due to the incision of the Tisza valley, which taps into the shallow groundwater [80]. Overall, the difference in water levels between the two studied periods is 1–5 m (Figure 14).

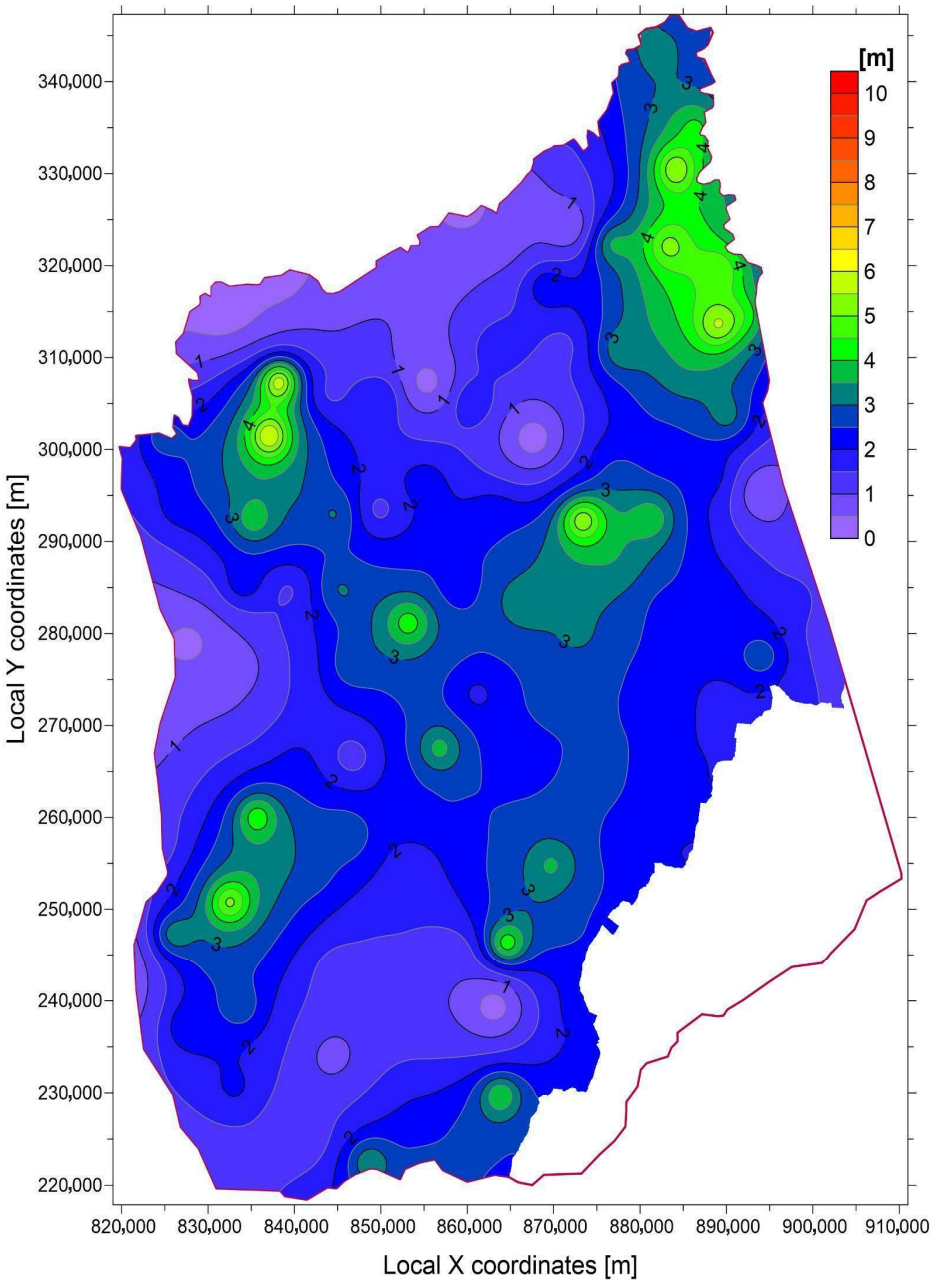

Figure 12. The minimum depth of summer groundwater level below the surface in metres (2010) in the Nyírség region was calculated using Kriging.

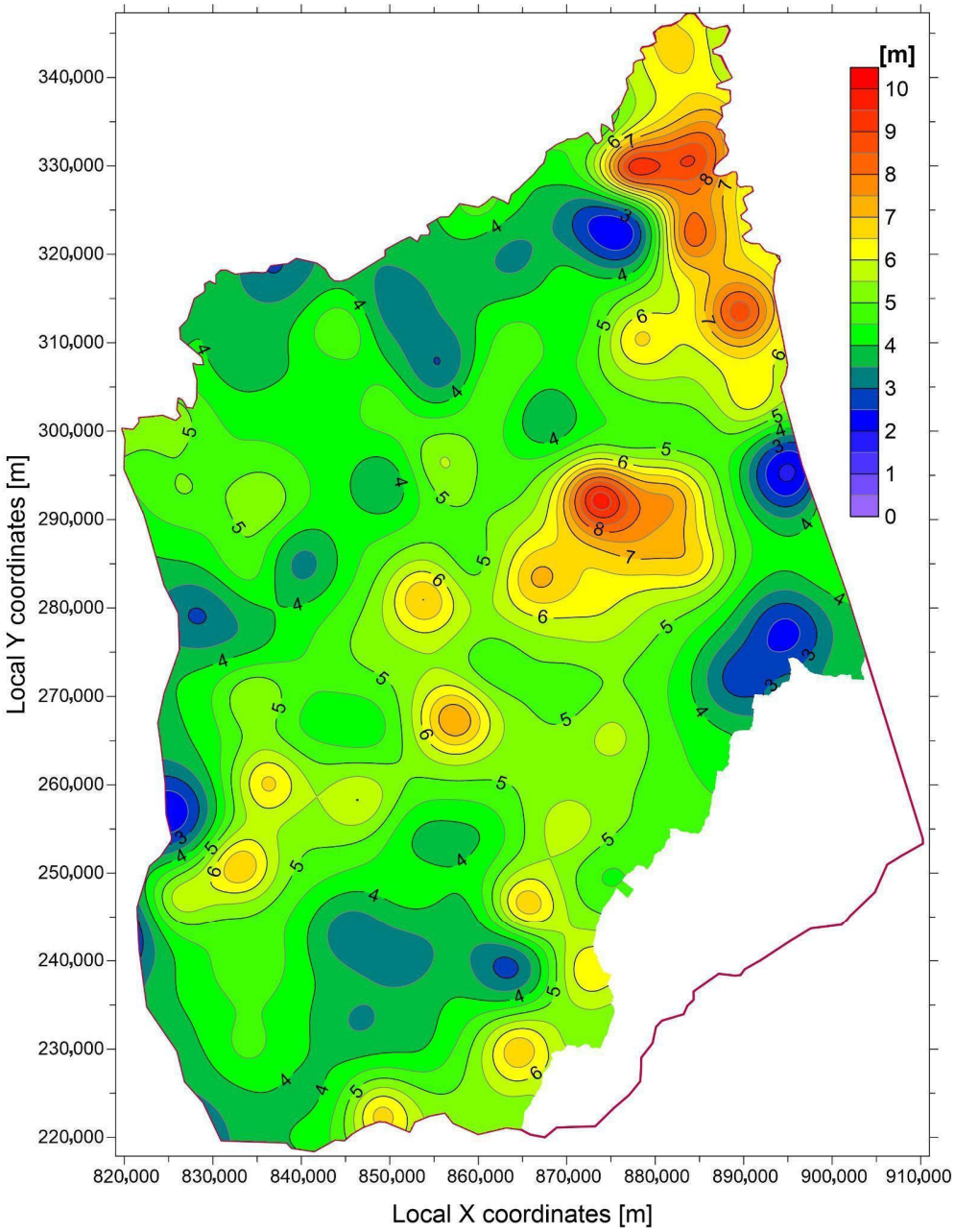

Figure 13. The maximum depth of summer groundwater level below the surface in metres (2022) in the Nyírség region was calculated using Kriging.

4.2. Changes in Water Production Data

To assess the impact of human activity on water resources, we must consider not only shallow groundwater but also the total water production of the Pleistocene aquifer, including legal and illegal withdrawals. A peculiarity of the Hungarian legal system is that it does not impose penalties for illegally constructed wells. In fact, an amendment to the law in 2023 does not require a permit for the construction of wells shallower than 50 m for agricultural or domestic use. Consequently, the estimated illegal water production in the Nyírség region exceeds legal production [9]. This estimate is made with the cooperation of the water authorities, using aerial photographs, satellite images and field surveys. Water production has grown steadily over the past 35 years (see Table 2).

Table 2. Legal and illegal water production data in the Nyírség region.

Time Period [Year]	Legal Water Production [m^3/Year]	Illegal Water Production [m^3/Year]	Total Water Production [m^3/Year]
1990–1994 [80]	35,294,025	40,000,000	75,294,025
2012–2018 [50]	42,022,974	48,600,000	90,622,974
2022	51,774,319	58,200,000	109,974,319

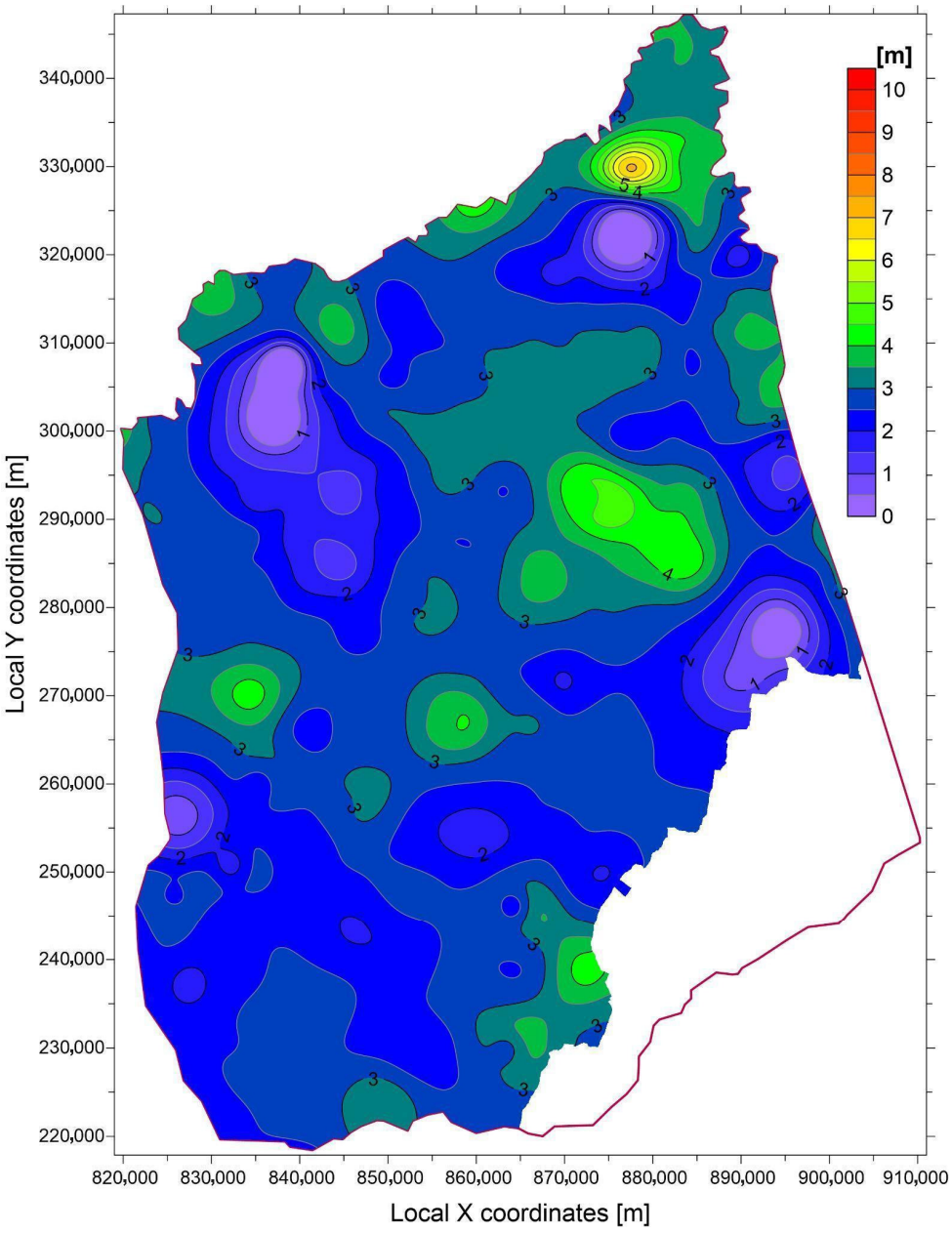

Figure 14. The difference in metres between the minimum and maximum depths of the summer groundwater level (2022 and 2010) below the surface in the Nyírség region.

We know the exact location and screened depth of all legally drilled wells. According to data from 2022, approximately 10% of legal production comes from the lower Pleistocene (shallow aquifer) layers, 23% from the middle Pleistocene layers and 67% from the most productive lower Pleistocene layers. However, as the exact location and depth of illegal wells are unknown, we developed the method presented in the following section.

4.3. Location of Illegal Wells, and Production

The national water-authority irrigated-parcel shapefile is treated as the primary 'ground-truth' mask for registered irrigated agriculture; NDVI and LST are used only as ancillary indicators to identify parcels that are actively vegetated and show relative surface cooling during the Landsat acquisition window. The workflow starts from a vector shapefile of irrigated field parcels, which defines the candidate agricultural area where unregistered abstraction is most plausible. For the peak growing season, NDVI and Land Surface Temperature (LST) were extracted from the Landsat 8 Level-2 (L2 T2) image collection for 10–26 July 2022. NDVI was computed from the normalized difference in the near-infrared (Band 5) and red (Band 4) bands, while LST was derived from the thermal band (Band 10) and converted to degrees Celsius. We applied a conservative NDVI screening window (0.4–0.6) to exclude bare soil and very sparse vegetation and to retain moderately vegetated agricultural parcels during the image window, consistent with standard NDVI interpretation [81].

For candidate illegal well delineation, the study area was split into six tiles to support systematic sampling and processing. NDVI and LST values were combined per tile and exported as comma-separated values (CSV) for cleaning and filtering; only samples meeting the cropland NDVI criterion (0.4–0.6) were retained. Potential well points were then generated around the centroids of irrigated-field polygons, applying spatial logic to reduce unrealistic clustering and edge effects: wells were enforced to be at least 1000 m apart, excluded for parcels smaller than 1000 m^2 or larger than 100,000 m^2, and avoided within 1000 m of water bodies and near the study-area boundary. To prevent conflicts with registered infrastructure, candidate wells within 500 m of known real wells were removed using geodesic distance filtering. Remaining candidates were categorized into three temperature classes using LST (Cold/Medium/Warm), with temperatures normalized to 5–16 °C (values above 16 °C capped) and exported as Categorized_temp.xyz (index 1 = cold/high potential, 2 = medium, 3 = warm/lower potential). A final exclusion step used land-cover shapefiles (forest, water bodies, wetlands) buffered by 100 m to remove candidate wells in restricted zones; coordinates were transformed from Hungarian EOV to WGS84, and the resulting filtered candidates and real wells were visualized in an interactive Folium map and exported to CSV for documentation and further analysis (Figure 15).

The resulting points represent candidate well locations rather than confirmed infrastructure. Uncertainty arises from sensor and processing effects in NDVI/LST (e.g., mixed pixels and temporal variability between acquisition dates), from the heuristic nature of threshold and distance rules (NDVI range, buffer distances, parcel-size limits), and from potential positional error or incompleteness in the registered well dataset used for exclusion. Therefore, the mapped candidates should be interpreted as hypotheses for follow-up verification, not as definitive detections.

4.4. Changes in Climate

Between 1981 and 2024, annual precipitation shows significant interannual variation, ranging from 896 mm (2010) as the wettest year to 450 mm (2022) as the driest year (Figure 16). Although the trend is not monotonic, no clear trend can be identified. The contribution of heavy-rainfall days (>25 mm day^{-1}) is highly episodic. It peaked at 213.3 mm in 1985 (approximately one third of the annual total) but was much lower in other years (e.g., 1986 and 2024; Figure 16), so the proportion of heavy rainfall tends to decrease with altitude.

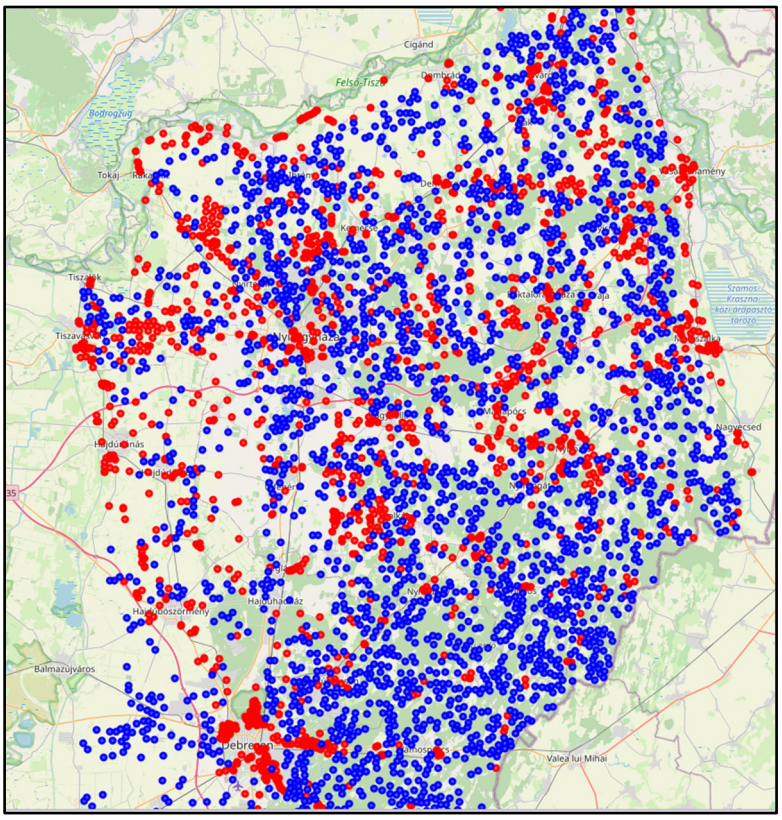

Figure 15. Spatial distribution of wells in the Nyírség region. Red points show legal wells, while blue points indicate generated potential illegal wells.

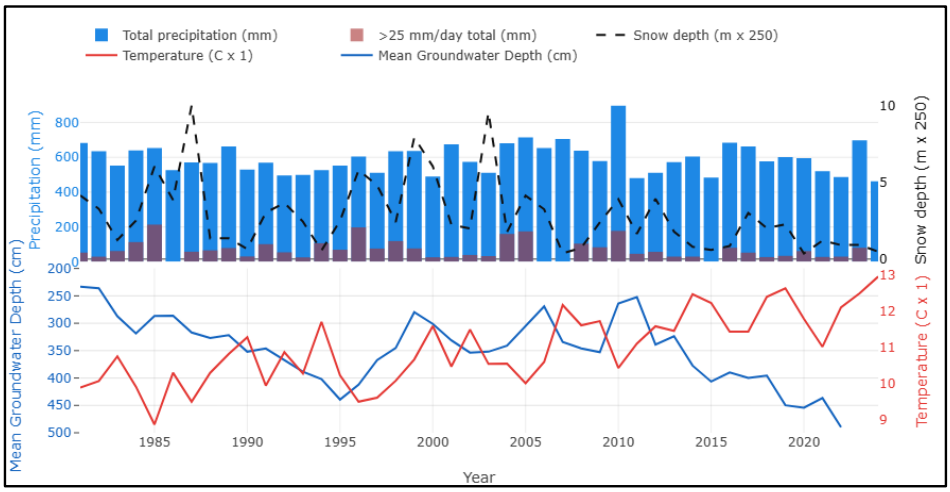

Figure 16. Annual precipitation and heavy-rain contribution (>25 mm day^{-1}) with snow depth and air temperature. Left axis bars show total annual precipitation (blue) and heavy-rain contribution (>25 mm day^{-1}, red). Right axis lines display annual mean snow depth (scaled × 250) and 2 m air temperature (scaled × 1), illustrating the relationship between heavy rainfall and cryospheric/thermal conditions.

The snow-depth indicator in Figure 16 (dashed black line; scaled ×250) shows a pronounced long-term decline, indicating reduced snow presence and persistence in the system: snow depth drops from 0.0166 m (1981) to ~0.0019 m (2024) (near-zero), with a maximum of 0.0401 m (1987) and a minimum of ~0.00145 m (2020), and the reduction is most evident during 2010–2024, when values remain consistently low. This loss of snow storage implies a shift in cold-season precipitation toward more rain-dominated inputs

and/or weaker accumulation and retention, reducing the snowpack's role as a seasonal water storage, compressing the timing of water release, and potentially shifting runoff earlier while weakening late-season hydrologic buffering [82].

Mean annual air temperature increased from 9.89 °C (1981) to 12.96 °C (2024), corresponding to a net warming of +3.08 °C over the observation period (Figure 16). The warmest conditions occur at the end of the record, while cooler years are concentrated early in the time series (e.g., minimum near the mid-1980s). The co-occurrence of higher temperatures and declining snow depth in the last 15 years supports the interpretation that warming has contributed to a reduced fraction of precipitation retained as snow and to earlier melt or diminished snow persistence [83,84].

From a water-balance perspective, warming is also expected to increase atmospheric evaporative demand and, consequently, potential evapotranspiration [83]. Higher air temperatures raise the capacity of the atmosphere to hold moisture and often increase vapor pressure deficits, which enhances the "drying power" of the atmosphere [85]. As a result, even when precipitation totals remain within the historical range, a warmer climate can reduce effective water availability by increasing evaporative losses from soils, open water, and vegetation (where water supply permits). Therefore, the warming trend evident in Figure 16 implies that hydrologic stress may intensify not only through changes in precipitation amount and phase (rain vs. snow), but also through enhanced evapotranspiration, which can reduce soil moisture, groundwater recharge potential, and summer baseflow—especially during low-precipitation years such as 2024.

4.5. Climate Change Forecast

Climate projections for Hungary indicate substantial warming in the Nyírség region by mid-century under all IPCC-consistent pathways. The magnitude depends on the scenario: low-emission pathways (e.g., SSP1-2.6/RCP2.6) suggest ~+1 °C warming by ~2050, intermediate pathways (e.g., SSP2-4.5/RCP4.5) suggest ~+1.5–2 °C, and high-emission pathways (e.g., SSP5-8.5/RCP8.5) approach ~+3 °C relative to late-20th-century conditions [86,87] (Figure 17). Note that the historical temperature series used here is based on observed annual-mean weather records, whereas the projections in Figure 17 are climate-model outputs summarized as 30-year daily averages; therefore, differences in baseline level (including the observed record appearing warmer than the modeled projections) reflect both methodological averaging and inherent observation–model differences rather than an inconsistency in the warming trend. Warming is expected to be strongest in summer and autumn, increasing the frequency and intensity of heat extremes and reducing cold conditions (i.e., fewer frost days)—a combination that increases evaporative demand and can intensify agricultural water stress [87]. In parallel, annual precipitation totals are generally projected to change only modestly by ~2050 (often within a few percent), yet the seasonal distribution is expected to shift toward drier summers and slightly wetter winters/autumns, with growing evidence for longer summer dry spells even when annual totals remain near historical levels [87]. Even without large annual changes, precipitation characteristics may become more variable, with a tendency toward more intense downpours and associated runoff/flood risk, particularly outside summer [87].

A robust signal across scenarios is the projected decline in snow depth and snow-cover duration by ~2050, driven primarily by warmer winters that reduce the fraction of precipitation falling and persisting as snow and increase winter rainfall [88]. For a lowland region such as Nyírség, this implies lower maximum snow depths, fewer snow days, and faster melt during cold-season warm spells, weakening the role of snow as seasonal water storage and shifting hydrologic timing toward more rain-dominated winter inputs [88]. In practice, reduced snow storage can diminish seasonal buffering

(less delayed release through snowmelt) and, when combined with warming-driven increases in atmospheric demand, can aggravate late-spring and summer water-availability constraints for groundwater-dependent irrigation systems [88,89]. Rybchynska et al. predict an 18% increase in evapotranspiration in the Carpathian Basin by 2050 [90], while we calculated a 25% increase in evapotranspiration for the Nyírség region, which is considered an extremely arid area. Kumar and his co-authors estimate a 20% decline in infiltration in Central Europe, which we also used in our forecast [91].

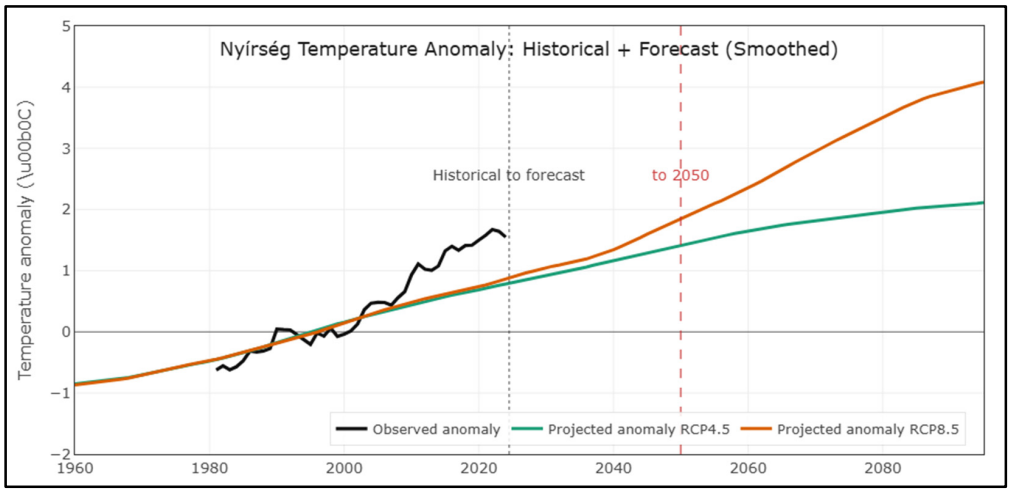

Figure 17. Bias-adjusted 2 m air temperature time series for the study area showing the observed baseline (black line; data-supported) and scenario-based projections (orange and green lines; RCP4.5 and RCP8.5) to mid-century, presented as 30-year daily moving-average values. Projected values represent conditional scenario outcomes rather than precise forecasts.

4.6. Numerical Model Setup

The model covers an area of 129 km north to south and 90.8 km east to west. During modeling, we used a grid size of 200 m. The model was divided vertically into seven layers (Figure 18): The uppermost layer (Layer 1) consists of mostly Holocene unconfined aquifers, underlain by Upper Pleistocene fine sandy aquifers (Layer 2), a clayey semi-aquitard with sand interlayers (Layer 3), middle Pleistocene sandy aquifer (Layer 4), a clayey aquitard (silt/clay) with sandy interlayers (Layer 5), and Lower Pleistocene sandy and coarse sandy aquifer, or waterworks layer (Layer 6). The lowermost layer (Layer 7) simulates the effect of wells under Pleistocene formations to determine lower boundary conditions (mostly Late Miocene sediments from Dunántúli Group). When determining the hydrogeological characteristics of the model layers, we considered the hydrogeological logs of the wells, as well as the outcomes of regional sequence stratigraphic studies [40–42] (Table 3). Potentiometric levels were determined using data from network monitoring (Figure 18).

The infiltration values used are proportional to the amount of precipitation that recharges the subsurface formations. Both the unsaturated zone and groundwater evapotranspiration, as well as vegetation water uptake, draw from these formations. This means that the infiltration value does not include surface runoff. In this case, infiltration is primarily dependent on topography, with values ranging from 120 to 250 mm per year (Figure 19). These values were slightly modified during calibration. In the base state of the model, the maximum evapotranspiration value at the surface was 708 mm per year, decreasing linearly to a depth of 5.8 m, at which point it reached 0. Rivers and major canals in the study area were incorporated into the model using hydrological longitudinal profiles.

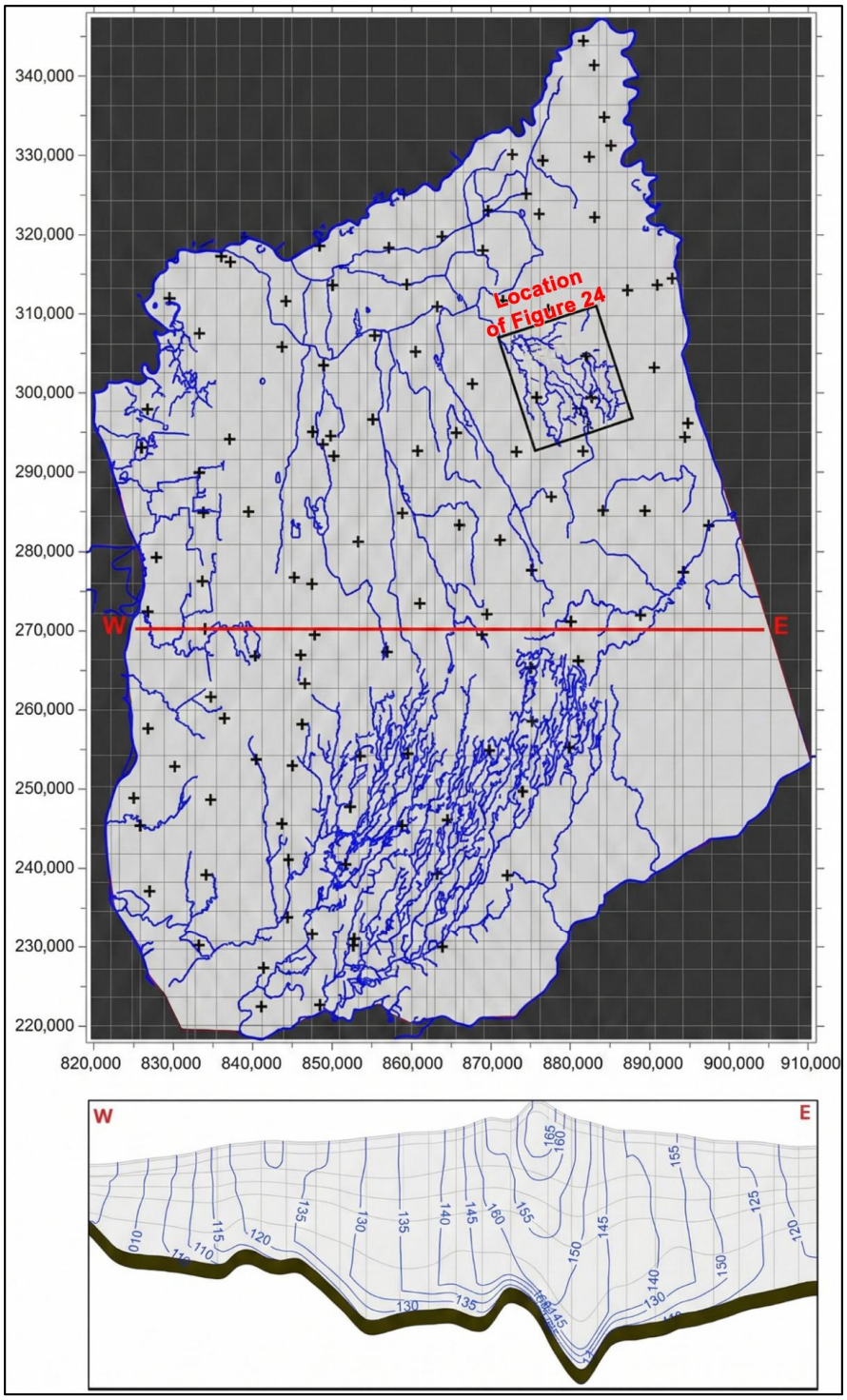

Figure 18. (**Top**) The model's grid with rivers and the trace of the vertical section. (**Bottom**) The west–east section of the model with equipotential lines [m]. Location of Figure 24 has been marked and labeled in this figure.

Table 3. Hydrodynamic parameters of model layers.

Model Layer Number	Horiz. Hydr.Conduct. K_h [m/d]	Vert. Hydr.Conduct. K_v [m/d]	Effective Porosity n_0
1.	0.23–0.91	0.049–0.23	0.2
2.	0.12–10.8	0.005–0.1	0.2

Table 3. *Cont.*

Model Layer Number	Horiz. Hydr.Conduct. K_h [m/d]	Vert. Hydr.Conduct. K_v [m/d]	Effective Porosity n_0
3.	0.17–1.93	0.001–0.012	0.08
4.	0.32–6.78	0.017–0.19	0.2
5.	0.34–4.71	0.0005–0.0075	0.06
6.	1.15–19	0.01–0.1	0.23
7.	0.1	0.001	0.15

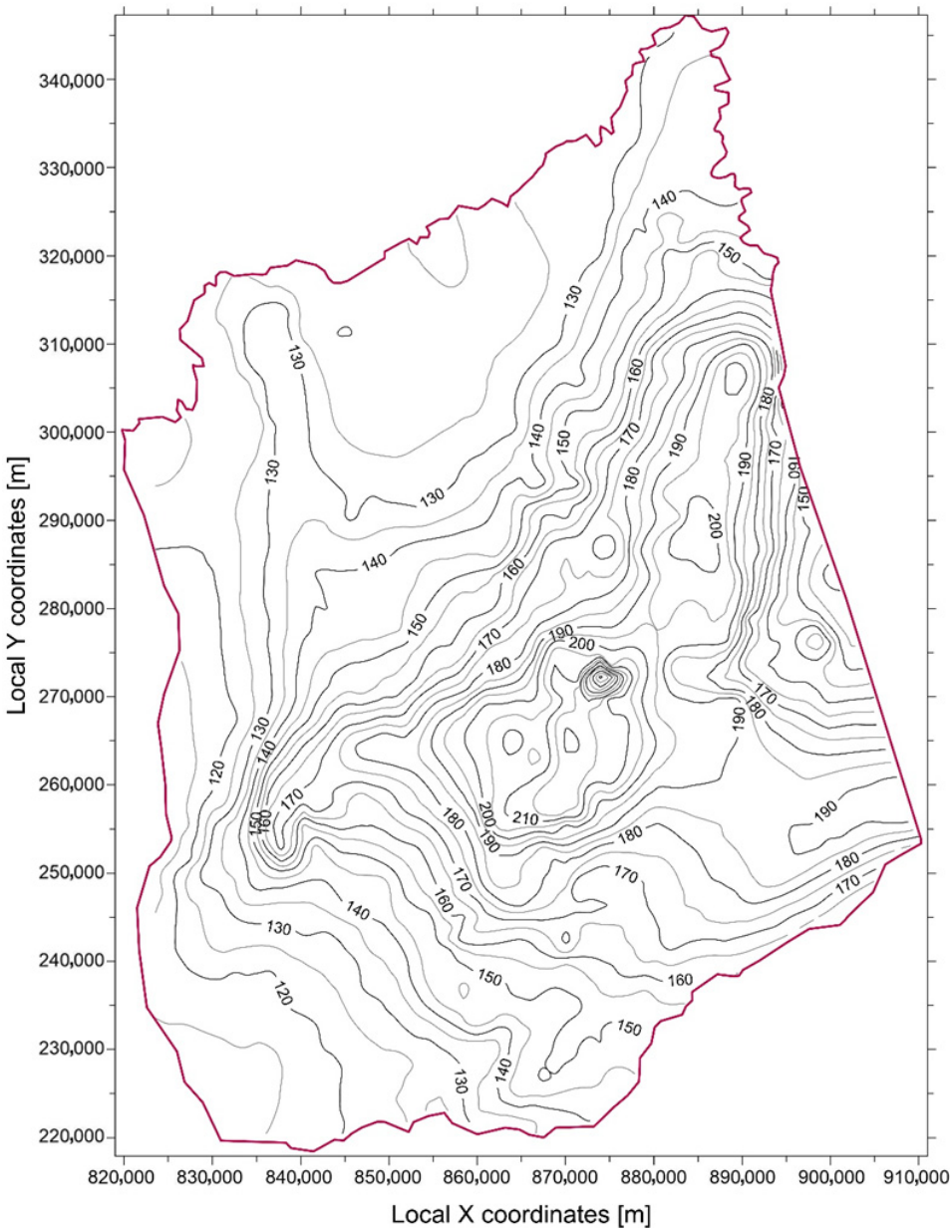

Figure 19. Infiltration values [mm/year] in the modeled area.

The most important consideration when selecting boundary conditions was to ensure that their effects influenced the calculation results as little as possible while maintaining stable water flow. Taking into account the natural boundaries of the groundwater level at the edges of the model—i.e., rivers—we only applied boundary conditions where

absolutely necessary to minimise disruption to water flow. However, for deeper layers, we had to specify a soft boundary condition (GHB), as the water flow at the boundaries is mostly horizontal. This boundary condition type also allows pressure level changes in the boundary cells if necessary, adjusting the water balance of the cell in proportion to the resulting depression. In the case of the lowest, 7th model layer, which represents the upper part of the Dunántúli Group (Late Miocene), it also ensures the lower openness of the model as a general-head boundary (GHB) boundary surface. Its value was set during calibration.

5. Discussion

5.1. Numerical Model Results and Forecast for 2050

Using the calibrated model, we ran simulations to work out the water levels for 2022, a period that is similar to the current situation (Figure 20). According to these results, the water level in shallow aquifers decreased by an average of 0.5–1.5 m compared to the 2010 period. The greatest decrease occurred in river valleys and elevated areas (Figure 21).

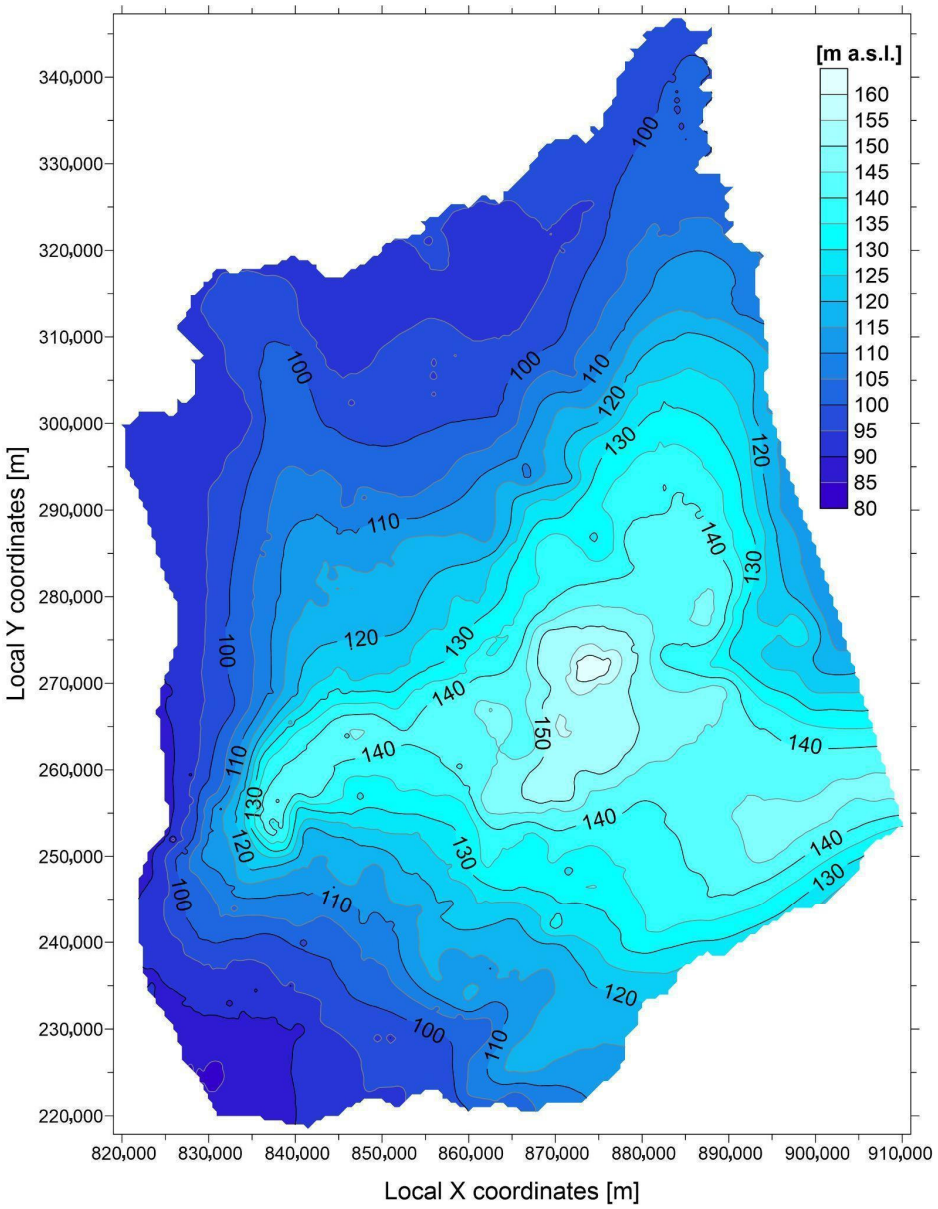

Figure 20. Shallow groundwater level in Nyírség area in 2022 (m a.s.l.).

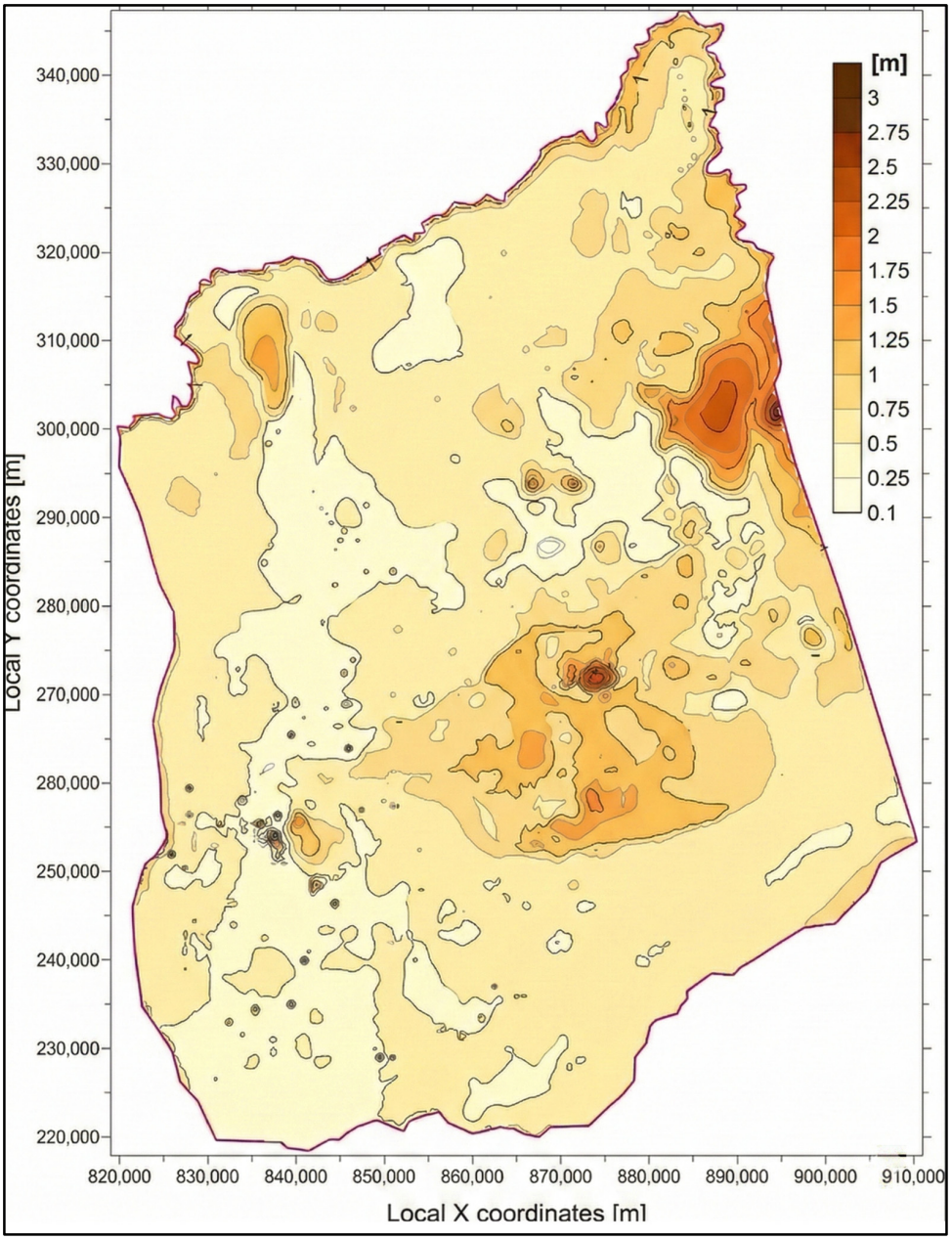

Figure 21. The extent of shallow groundwater level decline (in meters) in the Nyírség region between 2010 and 2022.

Based on the calculations of Kovács and Jakab [92] and the climate scenarios presented, we estimate a 20% decrease in infiltration by 2050. Meanwhile, evapotranspiration is expected to increase by 25% compared to the current dry season. To compensate for this, we anticipate that water production will increase by around 20%. We have created a separate model to illustrate and compare the effects of climate change and increased water production.

According to the model that simulates extreme dry climatic periods, a decrease in the level of shallow groundwater of more than 0.25 m is expected in most of the studied area. However, in regions with significantly higher elevations, this value may reach up to 1.25 m (see Figure 22A).

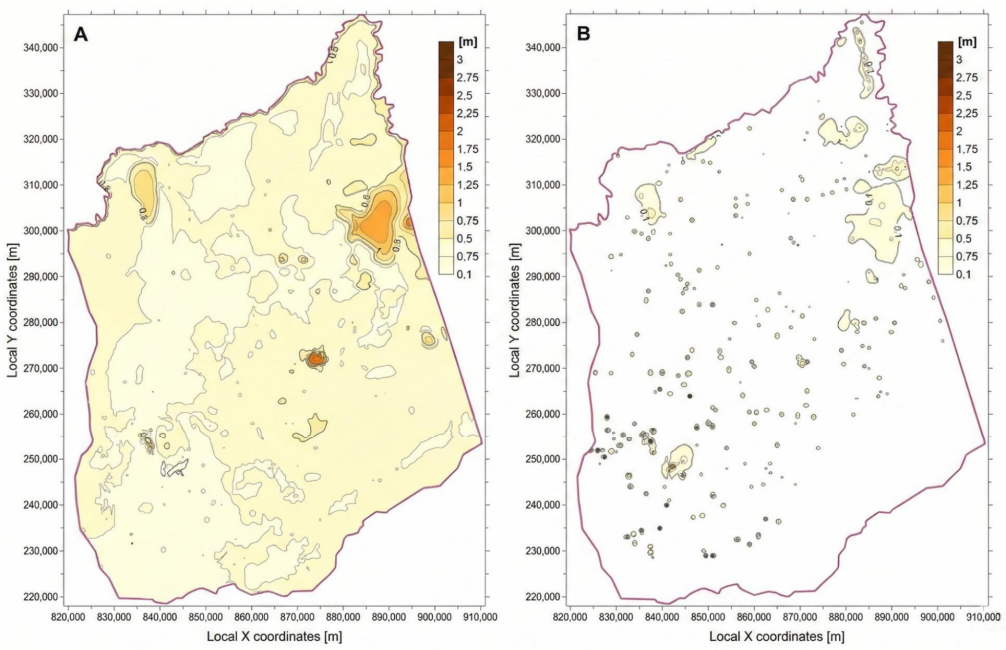

Figure 22. (**A**) The extent of the decline in shallow groundwater levels (in metres) in the Nyírség region under extreme drought climatic conditions in 2050; (**B**) The extent of the decline in shallow groundwater levels (in metres) in the Nyírség region in the event of a 20% increase in water withdrawal.

In the next model variant, we increased the production at all wells by 20% without changing their locations. In this case, the largest part of the model area experiences a decrease in the shallow groundwater level of less than 0.1 m, with the greatest reductions occurring at significant water extraction sites located in the recharge area. This is particularly true of Debrecen, the largest settlement in the area. Significant water production takes place there, accounting for around 10% of the total water extraction in the Nyírség region. Here, the rate of water level decline due to water production is close to the rate of water level decline due to climatic effects (Figure 22B).

Analysis of water budget data shows that, although maximum evapotranspiration is 25% higher during periods of extreme drought, the lower infiltration rate and decrease in groundwater levels mean the total amount is still lower. Under dry climatic conditions (in 2022), it is 1933 million m^3 per day; under extremely dry conditions (in 2050), it is 1521 million m^3 per day. This has led to a greater degree of atmospheric drought, i.e., a significant decrease in humidity. If extremely dry conditions persist, the levels of the middle and lower Pleistocene aquifers (model layers 4 and 6) will decrease slightly due to leakage in the groundwater flow system (Figure 23).

5.2. Proposed Actions Using a Numerical Model

By determining the amount of water lost due to the drop in shallow groundwater levels caused by extreme drought, we can estimate the scale of the artificial water replenishment task. First, we used the Surfer program to determine the volume of water that had decreased in the shallow aquifer. Between 2010 and 2022 this equated to 5.21 km^3, which, when the area of Nyírség is taken into account, represents an average decrease in the water level of 102 cm. Assuming 20% porosity, this volume equates to a water shortage of 1042 million m^3. Due to an error margin of approximately 15% in the determination of the water level, and the decline in water levels over several years, nearly the entire porosity may be depleted. Based on this, the missing total groundwater volume is 6 km^3, and the maximum porosity is 0.3, meaning the maximum missing water volume is approximately 1800 million m^3. The minimum value is 4.43 km^3 of missing total groundwater, calculated with a porosity of

0.18, meaning a water shortage of 800 million m^3. According to our forecast, an additional 2.55 km^3 of water will have been depleted by 2050. Assuming 20% porosity, this equates to a water shortage of 510 million cubic metres, corresponding to an average decrease in water levels in the shallow aquifer of 50 cm. Taking the above-mentioned uncertainty into account, the minimum water shortage is estimated to be 400 million m^3 and the maximum water shortage is estimated to be 880 million m^3. In other words, looking ahead to 2050, the impact of climate change since 2010 will result in a water shortage equivalent to more than ten times the annual water production. This cannot be artificially replenished, so the impact can only be reduced. MAR technology has long-term positive effects on groundwater resources, providing economic, social and environmental benefits [93]. In this study, we simulated two MAR options: (i) infiltration from surface reservoirs and (ii) subsurface injection through wells.

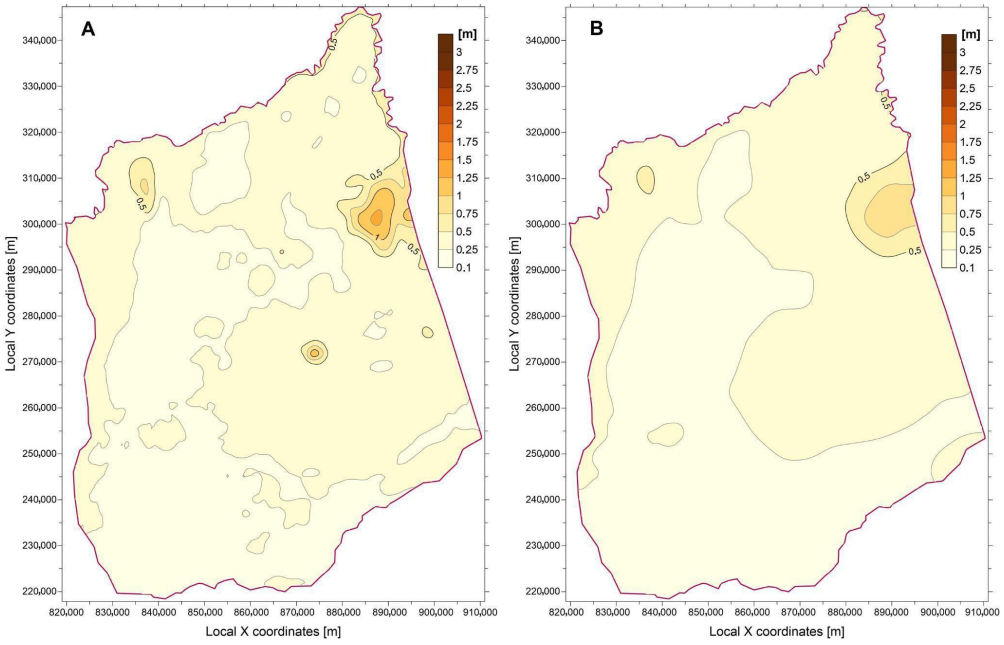

Figure 23. (**A**) The extent of the decline in groundwater level of middle Pleistocene aquifer (model layer 4); (**B**) The extent of the decline in groundwater level of lower Pleistocene aquifer (model layer 6) in metres in the Nyírség region under continuous extreme drought climatic conditions in 2050.

5.3. MAR—Replenishment of Rivers and Lakes

The water management authorities have developed plans for possible water replenishment. To simulate one of these proposals, we selected a 15 km × 13 km area in the north-eastern part of the model and rotated it by 18 degrees. This ensured that the western and eastern edges were perpendicular to both the surface slope and the equipotential lines. (Figure 24) [10]. To better observe changes in the water level, we used a vertical resolution of 10 m and a horizontal resolution of 5 m. We then examined the effect of changes in the surface water drainage system (2 lakes and 2 channels) on shallow groundwater in the area. Studying the longitudinal profiles of the channels, we modelled a 1 m rise for the channels and a 1.5 m rise for the lakes [18,94]. We did not allocate the necessary structures and assumed that water would be transported to the highest areas via pipelines, then released at a planned flow rate of 3–5 m^3/s. We determined the hydraulic conductivity of the colmated lake sediments to be 0.001 m/d, with a thickness of 0.5 m. For the 2 m-wide channels, these values are 0.0024 m/d and 0.33 m, respectively. The channels were modelled using the Stream package.

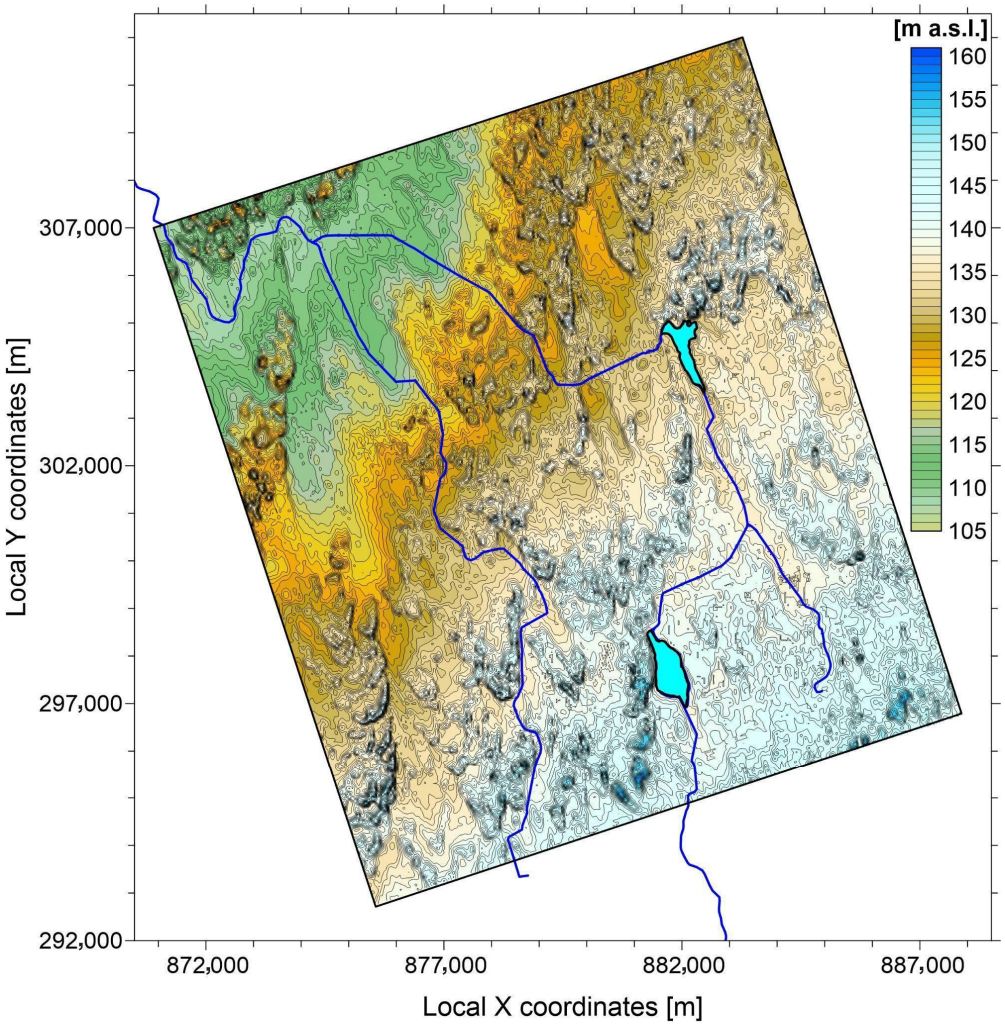

Figure 24. The terrain of the model area was examined in detail to show the channels and lakes that were taken into account in the simulation (See Figure 18 for the location of the area).

The results are shown in Figure 25. In the bands parallel to the channels, the water level rises by a few decimetres, whereas in the lakes it rises by 1 m. The edge of the impact area was defined as a rise of 5 cm, which, in constant modelling, is 180–300 m from the channel. In the case of lakes, this value is 800–1200 m. Lower values occur in northern lakes, while higher values occur in southern lakes.

To achieve a more realistic result, we performed transient modelling over a period of five years. Each year, water replenishment took place for four months using the values specified in the permanent model. For the remaining eight months, there was no water replenishment, and evaporation increased by 25%. As expected, the shallow groundwater level gradually rose at the end of the replenishment periods (Figure 26), as confirmed by the time series data of virtual observation wells located 1, 25, 75, 175 and 375 m from the lakes (Figure 27). Although the rise in shallow groundwater levels reached one metre in the immediate vicinity of the lakes, its influence only extended 150–400 m by the end of the fifth replenishment period (Figure 26c). In contrast, the rise in water levels in the canals was barely detectable. By the end of the dry period in the fifth year, the rise in water levels in the vicinity of the lakes was 0.2–0.3 m, shifting in a west-northwest direction corresponding to the direction of groundwater flow (Figure 26d).

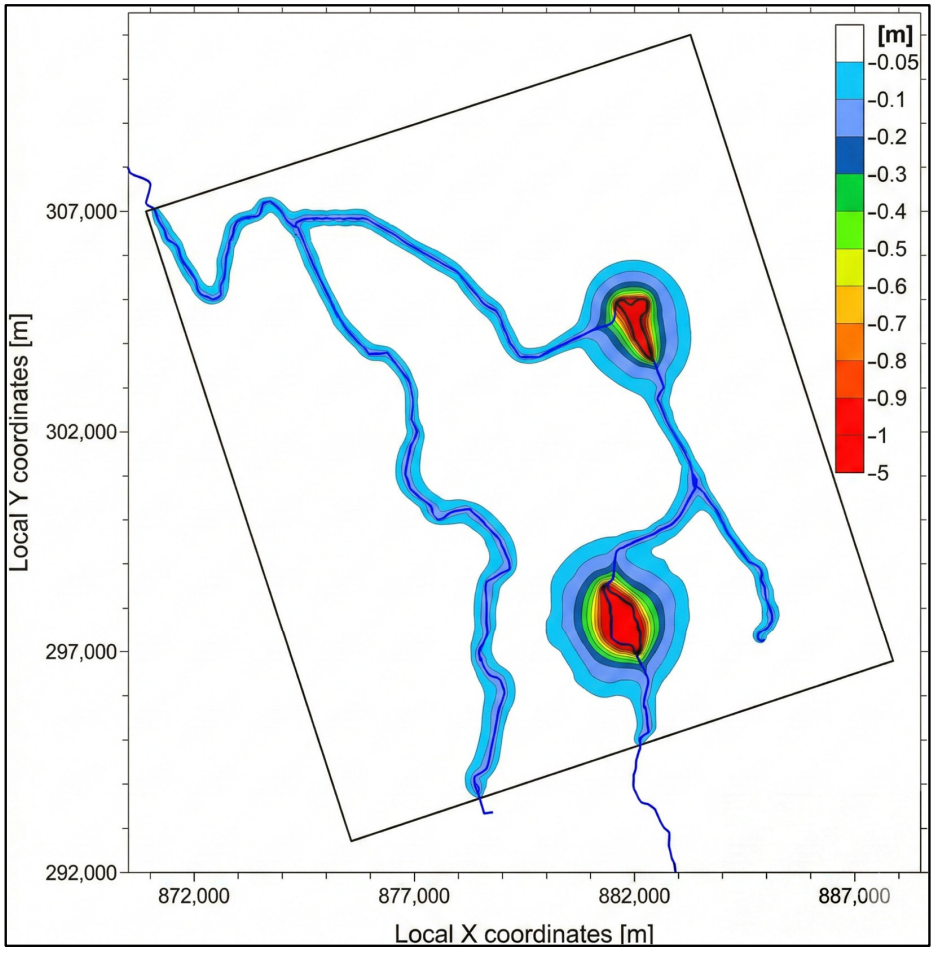

Figure 25. The value of groundwater depression due to permanent water recharge in channels and lakes (Negative values indicate a rise in water level).

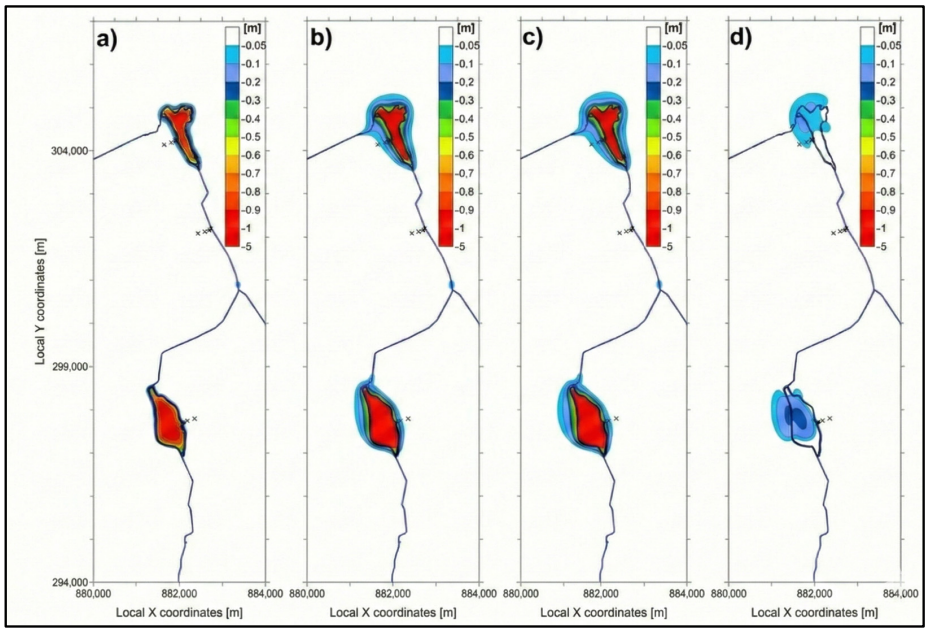

Figure 26. The value of groundwater depression due to water recharge in channels and lakes in the case of transient simulation: (**a**) after the end of the first replenishment period; (**b**) after the end of the third replenishment period; (**c**) after the end of the fifth replenishment period; (**d**) after the end of the fifth dry period (Negative values indicate a rise in water level). The crosses (x) indicate the location of observation wells.

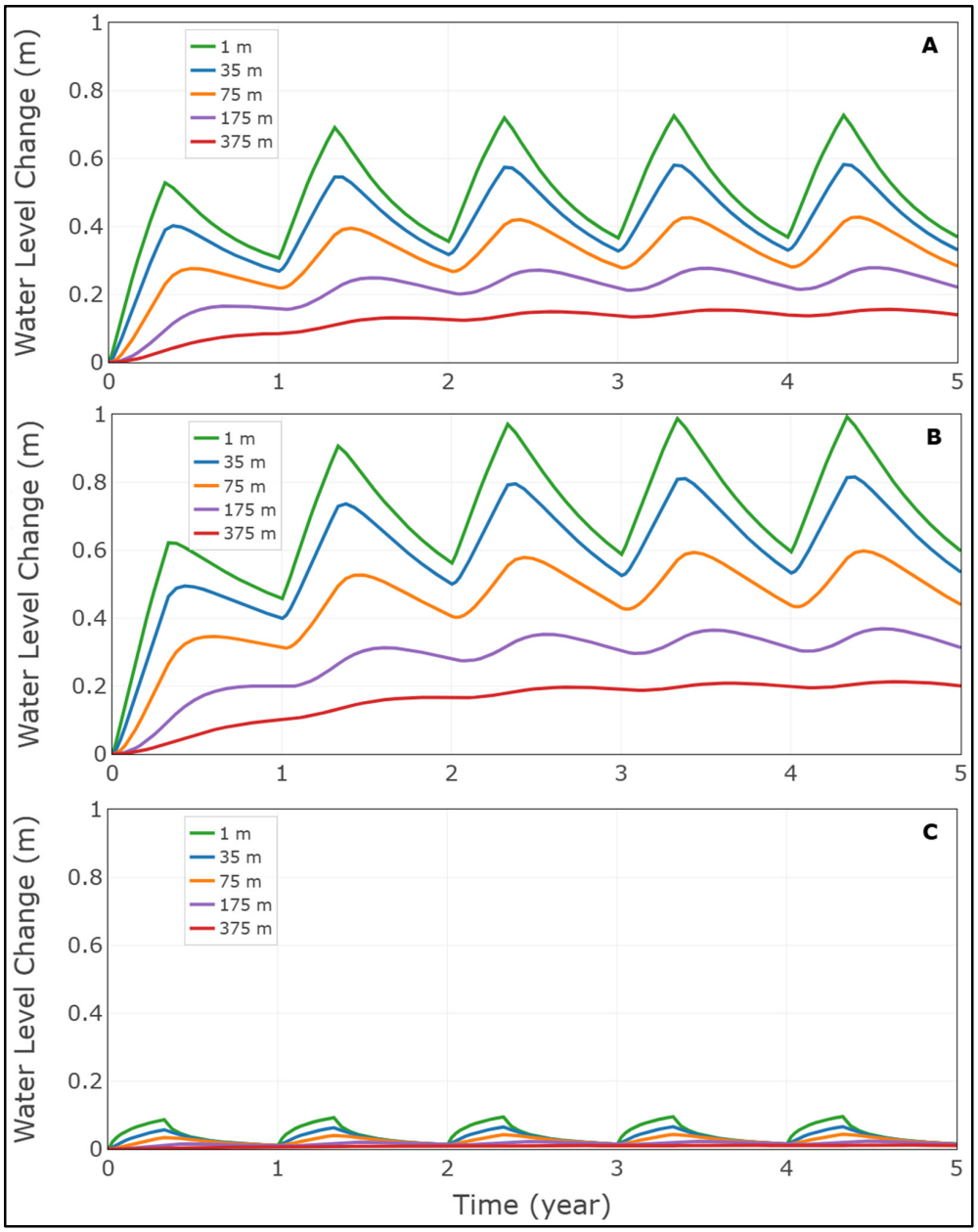

Figure 27. Water level changes in virtual observation wells at different distances from the transient water replenishment location over time: (**A**) near the northern lake; (**B**) near the southern lake; (**C**) near the channel between the lakes (see the location of the observation wells on Figure 26).

5.4. MAR—Subsurface Water Recharge

The amount of water infiltrating and evaporating can be determined using the water budget based on the infiltration through lakes method presented in the previous subsection. Using the drainage injection method to inject this total amount of water directly below the surface can increase the amount of water feeding the groundwater by around 30%.

We modelled this case by injecting the amount of water infiltrating and evaporating from the northern lake, as calculated in the previous model, into a drainage system located near the lake and used for infiltration in the previous scenario, rather than into the lake itself. The drain was set to a length of 3 × 700 m to ensure that the maximum rise in water level would not exceed 5 m. In this case, the effective range of artificial water recharge, which raises the water level by at least 5 cm, increased from 800–100 m to 1000–1250 m (Figure 28).

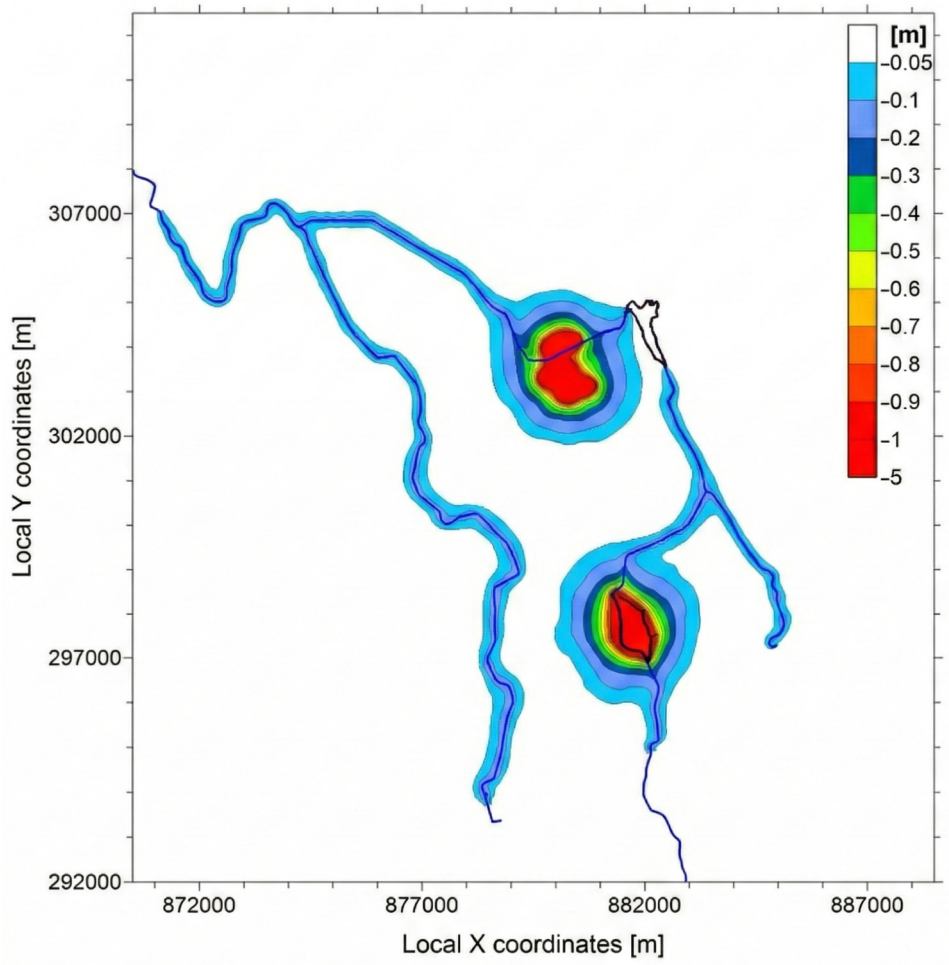

Figure 28. Groundwater-level change (depression map; negative values indicate a rise) under the permanent subsurface recharge (drainage injection) scenario near the northern lake area.

When interpreting the results, the uncertainty identified during calibration (see Section 3.3) must be taken into account. This is particularly significant in the case of channels. Therefore, the results can be used primarily to compare different MAR methods; in other words, they are useful for identifying trends.

5.5. Changing the Agricultural Cultivation System

Numerous studies have examined changes in groundwater levels in the Carpathian Basin caused by climate change [31,32,88,92]. However, in recent years, particularly over the past five years, water levels have declined by more than forecast. According to our simulations based on climate change projections, the situation will continue to deteriorate, with groundwater levels falling even further by 2050.

To improve groundwater decision-making in the Nyírség region, we recommend moving toward a data-driven groundwater management system that integrates monitoring and operational information into a single, continuously updated workflow [95–98]. The key rationale is that the main stressors—possible overextraction, limited/uneven monitoring coverage, and climate-driven variability in recharge and demand—cannot be evaluated reliably when data remain fragmented across institutions, formats, and time scales. As a practical first step, the existing digital platform developed for the General Directorate of Water Management of Hungary (which already compiles historical well information and annual/monthly abstraction records for the Nyírség area) should be strengthened as a shared data infrastructure (standardized identifiers, quality control, consistent time steps, and spatial referencing) [99,100]. We suggest that this infrastructure be designed

explicitly to support an updatable groundwater "digital twin"—a model framework that is periodically recalibrated with new groundwater levels, pumping volumes, and relevant hydroclimatic drivers—so that resource status can be tracked in near-real time and management actions can be evaluated against measurable indicators (e.g., groundwater-level thresholds and trend-based early warnings) [82,101,102].

Building on this foundation, we further recommend that the system be used not only for monitoring but also to optimize the agricultural cultivation system in terms of water efficiency by translating hydrogeologic constraints into extraction limits and operational guidance. Concretely, the digital twin can be used to define adaptive caps (monthly/seasonal/annual) on allowable abstraction at the well or management-unit scale, triggered by groundwater-level thresholds and expected seasonal recharge, and then link these limits directly to irrigation operations [99,100,103]. In parallel, the platform should monitor agricultural variables that strongly control water demand—especially crop type, cultivated area, and cropping calendar—and generate recommendations that improve water efficiency (e.g., irrigation scheduling, application-efficiency improvements, and allocation rules) while remaining within the extraction caps. Importantly, crop selection should be treated as part of the decision-support loop: the system can support recommendations to avoid or restrict high water-demand crops in stressed areas or dry years and instead encourage more water-efficient or drought-tolerant crop types/varieties, thereby aligning permitted groundwater withdrawals with crop water requirements and reducing the risk that agricultural planning drives unsustainable groundwater abstraction [21,22,104].

6. Conclusions

This study combines multi-decadal shallow-groundwater monitoring (1970–2022), hydroclimate indicators from CHIRPS and ERA5-Land (1981–2024), and a calibrated MODFLOW groundwater-flow model to quantify how climate variability/change and groundwater abstraction have affected the Nyírség recharge–discharge system and to evaluate realistic management options.

Observations and simulations consistently show that shallow groundwater decline has intensified since 2010, especially in the higher-elevation recharge areas (>~125–130 m). Individual wells record declines of up to ~3 m, and wet–dry spatial mapping between June 2010 and September 2022 indicates regional differences of ~1–5 m in groundwater depth. Model results further indicate that 2022 shallow-groundwater levels were, on average, ~0.5–1.5 m lower than in 2010. Over the same hydroclimatic period, precipitation remained highly variable (450–896 mm/year), but the system experienced pronounced warming (~3.1 °C increase in mean annual air temperature over 40 years, 1.8 °C of which occurred in the last 15 years) and a strong reduction in snow storage (mean snow depth from 0.0166 m in 1981 to ~0.0019 m in 2024), implying higher evaporative demand and reduced cold-season water availability for recharge.

Scenario analysis suggests that mid-century groundwater conditions will be dominated by climate-driven stresses. Under the "extreme drought" scenario applied here (−20% infiltration and +25% evapotranspiration), shallow groundwater declines by >0.25 m across most of the model domain and reaches up to ~1.25 m in the elevated recharge zone by 2050. A +20% increase in pumping produces comparatively small additional regional decline (<0.1 m across most of the area) but creates localized drawdown hotspots near major pumping centres (e.g., Debrecen) where pumping impacts can approach the magnitude of climate impacts. Expressed as a storage deficit, the estimated groundwater depletion between 2010 and 2022 is 4.43–6 km^3, with levels expected to decline by a further 2–3 km^3 by 2050. Taking the lowest porosity value into account, the total estimated deficit between 2010 and 2050 is over ten times the amount of groundwater

produced in 2022. This shows that deficits at the basin level cannot be fully compensated for by technical interventions alone and that they can be managed more effectively through mitigation and strategic localisation.

Managed aquifer recharge (MAR) can provide meaningful but primarily local benefits. Surface-water recharge via lakes and channels produces measurable rises—decimetres near channels and up to ~1 m near lakes—yet the radius of influence remains limited (steady-state ~0.18–0.30 km for channels and ~0.8–1.2 km for lakes for a 5 cm rise; transient lake influence ~0.15–0.40 km by year 5), with canals often showing minimal detectable effects. In contrast, direct subsurface recharge (drainage injection) increases the 5 cm influence radius to ~1.0–1.25 km and improves effective replenishment by ~30% relative to the surface-lake infiltration case, making it the preferred MAR option where source water and infrastructure are feasible. These findings point to clear management priorities: withdrawals must be measurable and enforceable (including explicitly accounting for unregistered abstraction estimated at 35–70 million m^3/year), demand-side measures should be prioritized through efficiency and adaptive caps triggered by groundwater thresholds (especially in recharge areas during dry years), and MAR should be targeted where it can work—favoring subsurface injection and local retention over basin-wide "replacement" strategies. Finally, institutionalizing an updatable decision-support workflow—a "digital twin" built on shared monitoring of levels, pumping, and hydroclimate drivers with periodic recalibration and transparent threshold-based indicators—offers the most robust pathway for early warning and for evaluating interventions as conditions evolve.

Therefore, to maintain the prosperity of the area, complex water resource management that takes both water use and land use into account is necessary.

Author Contributions: Conceptualization, J.S., H.A.A., R.H., É.S. and L.L.; methodology, J.S., H.A.A. and R.H.; software, J.S., H.A.A. and E.T.; validation, J.S. and E.T.; formal analysis, J.S. and H.A.A.; investigation, J.S. and H.A.A.; resources, J.S., H.A.A. and R.H.; data curation, J.S., H.A.A., R.H. and T.G.; writing—original draft preparation, J.S., H.A.A. and R.H.; writing—review and editing, J.S., H.A.A. and R.H.; visualization, J.S., H.A.A., T.G. and E.T.; supervision, J.S. and H.A.A.; project administration, R.H., É.S. and L.L.; funding acquisition, R.H. All authors have read and agreed to the published version of the manuscript.

Funding: This research was funded by the European Union and the Government of Hungary under the Recovery and Resilience Facility (RRF) within the Széchenyi Plan Plus Programme, Project No. RRF-2.3.1-21-2022-00008 (National Laboratory for Water Science and Water Security/Víztudományi és Vízbiztonsági Nemzeti Laboratórium).

Data Availability Statement: The data supporting the findings of this study are restricted due to confidentiality reasons and are therefore not publicly available. The code and some open source data used for data processing and analysis are publicly available on Zenodo, which is already cited in the manuscript and includes the corresponding link. https://doi.org/10.5281/zenodo.17912092; https://doi.org/10.5281/zenodo.17911943.

Acknowledgments: The authors gratefully acknowledge the support of the General Directorate of Water Management (Országos Vízügyi Főigazgatóság—OVF), the Upper-Tisza Regional Water Directorate (Felső-Tisza-vidéki Vízügyi Igazgatóság—FETIVIZIG), and the Trans-Tisza Region Water Directorate (Tiszántúli Vízügyi Igazgatóság—TIVIZIG), as well as their teams, for assistance that supported this study. We also acknowledge Google Earth Engine for providing the computing platform used in this research. The authors additionally acknowledge the University of Szeged Library for covering the article processing charge (APC) of this manuscript. Regional climate model projections used were obtained from the open-access EURO-CORDEX initiative and are gratefully acknowledged.

Conflicts of Interest: The authors declare no conflicts of interest. The funders had no role in the study design; in the collection, analysis, or interpretation of data; in the writing of the manuscript; or in the decision to publish the results.

References

1. Ecosystem-Based Water Security and the Sustainable Development Goals (SDGs). Available online: https://www.conservation.org/research/ecosystem-based-water-security-and-the-sustainable-development-goals-(sdgs) (accessed on 17 December 2025).
2. Mishra, B.K.; Kumar, P.; Saraswat, C.; Chakraborty, S.; Gautam, A. Water Security in a Changing Environment: Concept, Challenges and Solutions. *Water* **2021**, *13*, 490. [CrossRef]
3. Omar, P.J.; Dwivedi, S.B.; Dikshit, P.K.S. Sustainable Development and Management of Groundwater in Varanasi, India. In *Advances in Water Resources Engineering and Management*; Alkhaddar, R., Singh, R.K., Dutta, S., Kumari, M., Eds.; Lecture Notes in Civil Engineering; Springer: Singapore, 2020; Volume 39, pp. 201–209.
4. Intergovernmental Panel on Climate Change (IPCC). *Chapter 8: Water Cycle Changes. Climate Change 2021: The Physical Science Basis*; Cambridge University Press: New York, NY, USA, 2023; Available online: https://www.ipcc.ch/report/ar6/wg1/chapter/chapter-8/ (accessed on 17 December 2025).
5. Intergovernmental Panel on Climate Change (IPCC). *Climate Change 2021—The Physical Science Basis: Working Group I Contribution to the Sixth Assessment Report of the Intergovernmental Panel on Climate Change*, 1st ed.; Cambridge University Press: Singapore, 2023.
6. Hidrológiai Közlöny. (98. Évfolyam). Könyvtár. Hungaricana. 2018. Available online: https://library.hungaricana.hu/hu/view/HidrologiaiKozlony_2018/?pg=260&layout=s (accessed on 17 December 2025).
7. Bartholy, J. Regional climate change expected in Hungary for 2071–2100. *Appl. Ecol. Environ. Res.* **2007**, *5*, 1–17. [CrossRef]
8. Jánosi, I.M.; Bíró, T.; Lakatos, B.O.; Gallas, J.A.C.; Szöllosi-Nagy, A. Changing Water Cycle under a Warming Climate: Tendencies in the Carpathian Basin. *Climate* **2023**, *11*, 118. [CrossRef]
9. Szabó, É.; Simonffy, Z. *A Fels\Ho-Tisza-Vidéki Vízügyi Igazgatóság Vízkészlet-Gazdálkodási Térségi Tervének Felülvizsgálata: Új Szabályozás Bevezetése a Felszín Alatti Vízkészletekkel Való Gazdálkodásban*; Hidrológiai Társaság: Budapest, Hungary, 2023.
10. Dillon, P.; Alley, W.; Zheng, Y.; Vanderzalm, J. (Eds.) *Managed Aquifer Recharge: Overview and Governance*; IAH Special Publication: Reading, UK, 2022.
11. Sufyan, M.; Martelli, G.; Teatini, P.; Cherubini, C.; Goi, D. Managed Aquifer Recharge for Sustainable Groundwater Management: New Developments, Challenges, and Future Prospects. *Water* **2024**, *16*, 3216. [CrossRef]
12. Nightingale, H.I.; Ayars, J.E.; McCormick, R.L.; Cehrs, D.C. Leaky Acres Recharge Facility: A Ten-Year Evaluation. *JAWRA J. Am. Water Resour. Assoc.* **1983**, *19*, 429–437. [CrossRef]
13. Kløve, B.; Ala-Aho, P.; Bertrand, G.; Gurdak, J.J.; Kupfersberger, H.; Kværner, J.; Muotka, T.; Mykrä, H.; Preda, E.; Rossi, P.; et al. Climate Change Impacts on Groundwater and Dependent Ecosystems. *J. Hydrol.* **2014**, *518*, 250–266. [CrossRef]
14. Wu, W.-Y.; Lo, M.-H.; Wada, Y.; Famiglietti, J.S.; Reager, J.T.; Yeh, P.J.-F.; Ducharne, A.; Yang, Z.-L. Divergent Effects of Climate Change on Future Groundwater Availability in Key Mid-Latitude Aquifers. *Nat. Commun.* **2020**, *11*, 3710. [CrossRef]
15. Bloomfield, J.P.; Marchant, B.P.; McKenzie, A.A. Changes in Groundwater Drought Associated with Anthropogenic Warming. *Hydrol. Earth Syst. Sci.* **2019**, *23*, 1393–1408. [CrossRef]
16. Taylor, R.G.; Scanlon, B.; Döll, P.; Rodell, M.; Van Beek, R.; Wada, Y.; Longuevergne, L.; Leblanc, M.; Famiglietti, J.S.; Edmunds, M.; et al. Ground Water and Climate Change. *Nat. Clim. Chang.* **2013**, *3*, 322–329. [CrossRef]
17. ERA5-Land Hourly Data from 1950 to Present. Available online: https://cds.climate.copernicus.eu/datasets/reanalysis-era5-land?tab=overview (accessed on 9 February 2026).
18. Harbaugh, A.W. *MODFLOW-2005: The U.S. Geological Survey Modular Ground-Water Model—The Ground-Water Flow Process*; Techniques and Methods 6-A16; U.S. Geological Survey: Reston, VA, USA, 2005. [CrossRef]
19. Abd El Ghany, M.M.; El-Hadidy, S.M.; Sakr, S.A.; Korany, E.A.; Morsy, S.M. Visual MODFLOW, Solute Transport Modeling, and Remote Sensing Techniques for Adapting Aquifer Potentiality under Reclamation and Climate Change Impacts in Coastal Aquifer. *Sci. Rep.* **2024**, *14*, 22827. [CrossRef]
20. Knowling, M.J.; Werner, A.D.; Herckenrath, D. Quantifying Climate and Pumping Contributions to Aquifer Depletion Using a Highly Parameterised Groundwater Model: Uley South Basin (South Australia). *J. Hydrol.* **2015**, *523*, 515–530. [CrossRef]
21. Chakraborti, R.; Davis, K.F.; DeFries, R.; Rao, N.D.; Joseph, J.; Ghosh, S. Crop Switching for Water Sustainability in India's Food Bowl Yields Co-Benefits for Food Security and Farmers' Profits. *Nat. Water* **2023**, *1*, 864–878. [CrossRef]
22. Dangar, S.; Mishra, V. Groundwater Sustainability in India through Nonrice-Dominated Cropping Pattern. *PNAS Nexus* **2024**, *3*, pgae378. [CrossRef] [PubMed]
23. Groundwater Sustainability Assessment Based on Socio-Economic and Environmental Variables: A Simple Dynamic Indicator-Based Approach—PMC. Available online: https://pmc.ncbi.nlm.nih.gov/articles/PMC9461433/ (accessed on 9 February 2026).

24. Gropius, M.; Dahabiyeh, M.; Al Hyari, M.; Brückner, F.; Lindenmaier, F.; Vassolo, S. Estimation of Unrecorded Groundwater Abstractions in Jordan through Regional Groundwater Modelling. *Hydrogeol. J.* **2022**, *30*, 1769–1787. [CrossRef]
25. HungaroMet Hungarian Meteorological Service. Homogenized Data: Gridded Data Series (Meteorológiai Adattár/ODP). Published: Dataset Portal Page (Online Resource). Available online: https://odp.met.hu/climate/homogenized_data/gridded_data_series/ (accessed on 24 February 2026).
26. Chiang, W.-H.; Kinzelbach, W. Processing Modflow: A Simulation System for Modeling Groundwater Flow and Pollution. Hamburg, Germany and Zürich, Switzerland. 1998. Available online: https://ethz.ch/content/dam/ethz/special-interest/baug/ifu/ifu-dam/softwares/pmwin/pm5.pdf (accessed on 24 February 2026).
27. Erdélyi, M. *A Magyar Medence Hidrodinamikája = Hydrodynamics of the Hungarian Basin*; VITUKI: Budapest, Hungary, 1979.
28. Marton, L. A Környezeti Izotópok Felhasználása a Nyírség Negyedkori Mélységbeli Vizeinek Kutatásában. Kandidátusi Értekezés, 1981.
29. Szanyi, J. Felszín Alatti Víztermelés Környezeti Hatásai a Dél-Nyírség Példáján. Ph.D. Thesis, Szegedi Tudományegyetem (SZTE), Szeged, Hungary, 2004.
30. Szanyi, J. The Influence of Lower-Boundary Condition on the Groundwater Flow System. *Acta Geol. Hung.* **2005**, *47*, 93–103. [CrossRef]
31. Rakonczai, J.; Fehér, Z. *A Talajvízkészlet Változásának Értékelése Hazánkban*; Viziterv Environ Kft: Nyíregyháza, Hungary, 2019.
32. Rakonczai, J.; Fehér, Z. A klímaváltozás szerepe az Alföld talajvízkészleteinek időbeli változásaiban. *Hidrol. Közlöny* **2015**, *95*, 1–15.
33. Tóth, J. A Theoretical Analysis of Groundwater Flow in Small Drainage Basins. *J. Geophys. Res.* **1963**, *68*, 4795–4812. [CrossRef]
34. Tóth, J. Hydraulic Continuity in Large Sedimentary Basins. *Hydrogeol. J.* **1995**, *3*, 4–16. [CrossRef]
35. Püspöki, Z.; Demeter, G.; Tóth-Makk, Á.; Kozák, M.; Dávid, Á.; Virág, M.; Kovács-Pálffy, P.; Kónya, P.; Gyuricza, G.; Kiss, J.; et al. Tectonically Controlled Quaternary Intracontinental Fluvial Sequence Development in the Nyírség–Pannonian Basin, Hungary. *Sediment. Geol.* **2013**, *283*, 34–56. [CrossRef]
36. Csontos, L.; Nagymarosy, A.; Horváth, F.; Kovác, M. Tertiary Evolution of the Intra-Carpathian Area: A Model. *Tectonophysics* **1992**, *208*, 221–241. [CrossRef]
37. Marton, L.; Szanyi, J. A talajvíztükör helyzete és a rétegvíz termelés kapcsolata Debrecen térségében. *Hidrol. Közlöny* **2000**, *80*, 3–13.
38. Horváth, F.; Tari, G. IBS Pannonian Basin Project: A Review of the Main Results and Their Bearings on Hydrocarbon Exploration. In *The Mediterranean Basins: Tertiary Extension within the Alpine Orogen*; Durand, B., Jolivet, L., Horváth, F., Séranne, M., Eds.; Geological Society Special Publications; The Geological Society: London, UK, 1999; Volume 156, pp. 195–213.
39. Horváth, F.; Cloetingh, S. Stress Induced Late-Stage Subsidence Anomalies in the Pannonian Basin. In *Dynamics of Extensional Basins and Inversion Tectonics*; Cloetingh, S., Ben Avraham, Z., Sassi, W., Horváth, F., Eds.; Elsevier: Amsterdam, The Netherlands, 1996; Volume 266, pp. 287–300.
40. Püspöki, Z.; Markos, G.; Fancsik, T.; Bereczki, L.; Kiss, L.F.; Thamó-Bozsó, E.; Krassay, Z.; Kovács, P.; McIntosh, R.W.; Vári, Z.; et al. A Quasi-Continuous Long-Term (5 Ma) Mid-European Mountain Permafrost Record Based on Fluvial Magnetic Susceptibility and Its Contribution to the Explanation of Plio-Pleistocene Glaciations. *Boreas* **2024**, *54*, 156–177. [CrossRef]
41. Püspöki, Z.; Kovács, I.J.; Fancsik, T.; Nádor, A.; Thamó-Bozsó, E.; Tóth-Makk, Á.; Udvardi, B.; Kónya, P.; Füri, J.; Bendő, Z.; et al. Magnetic Susceptibility as a Possible Correlation Tool in Quaternary Alluvial Stratigraphy. *Boreas* **2016**, *45*, 861–875. [CrossRef]
42. Püspöki, Z.; Fogarassy-Pummer, T.; Thamó-Bozsó, E.; Falus, G.; Cserkész-Nagy, Á.; Szappanos, B.; Márton, E.; Lantos, Z.; Szabó, S.; Stercel, F.; et al. High-resolution Stratigraphy of Quaternary Fluvial Deposits in the Makó Trough and the Danube-Tisza Interfluve, Hungary, Based on Magnetic Susceptibility Data. *Boreas* **2021**, *50*, 205–223. [CrossRef]
43. Borsy, Z. *A Nyírség Természeti Földrajza*; Akadémiai Kiadó: Budapest, Hungary, 1961.
44. Flores, Y.G.; Eid, M.H.; Szűcs, P.; Szőcs, T.; Fancsik, T.; Szanyi, J.; Kovács, B.; Markos, G.; Újlaki, P.; Tóth, P.; et al. Integration of Geological, Geochemical Modelling and Hydrodynamic Condition for Understanding the Geometry and Flow Pattern of the Aquifer System, Southern Nyírség–Hajdúság, Hungary. *Water* **2023**, *15*, 2888. [CrossRef]
45. Nádor, A.; Sztanó, O. Lateral and Vertical Variability of Channel Belt Stacking Density as a Function of Subsidence and Sediment Supply: Field Evidence from the Intramountaine Körös Basin, Hungary. In *From River to Rock Record*; SEPM Special Publications: Claremore, OK, USA, 2010; Volume 99.
46. Kőrössy, L. A zalai-medencei k?olaj- és földgázkutatás földtani eredményei. *Ált. Földt. Szle.* **1988**, *23*, 3–162.
47. Rónai, A. Az Alföld tájai. In *Geologica Hungarica*; Rónai, A., Ed.; Series 21; Műszaki Könyvkiadó: Budapest, Hungary, 1985; pp. 258–407.
48. Almási, L.; Szanyi, J. Hydrogeology of the Pannonian Basin. In *The Groundwater Project and eBooks—Important Aquifer Systems Around The World*; The Groundwater Project: Guelph, ON, Canada, 2024.
49. Tóth, J.; Almási, I. Interpretation of Observed Fluid Potential Patterns in a Deep Sedimentary Basin under Tectonic Compression: Hungarian Great Plain, Pannonian Basin. *Geofluids* **2001**, *1*, 11–36. [CrossRef]
50. Tóth, G.; Kun, É.; Kerékgyártó, T. *Szabolcs-Szatmár-Bereg Megye Mintaterületére Készült Vízkészletgazdálkodási Modell*; Hungarian Water Management Authority: Budapest, Hungary, 2021.
51. Gorelick, N.; Hancher, M.; Dixon, M.; Ilyushchenko, S.; Thau, D.; Moore, R. Google Earth Engine: Planetary-Scale Geospatial Analysis for Everyone. *Remote Sens. Environ.* **2017**, *202*, 18–27. [CrossRef]

52. Funk, C.; Peterson, P.; Landsfeld, M.; Pedreros, D.; Verdin, J.; Shukla, S.; Husak, G.; Rowland, J.; Harrison, L.; Hoell, A.; et al. The Climate Hazards Infrared Precipitation with Stations—A New Environmental Record for Monitoring Extremes. *Sci. Data* **2015**, *2*, 150066. [CrossRef]
53. Muñoz-Sabater, J.; Dutra, E.; Agustí-Panareda, A.; Albergel, C.; Arduini, G.; Balsamo, G.; Boussetta, S.; Choulga, M.; Harrigan, S.; Hersbach, H.; et al. ERA5-Land: A State-of-the-Art Global Reanalysis Dataset for Land Applications. *Earth Syst. Sci. Data* **2021**, *13*, 4349–4383. [CrossRef]
54. Golden Software Golden Software Grid (.GRD) File Description. Available online: https://grapherhelp.goldensoftware.com/subsys/subsys_gsi_grd_file_format.htm (accessed on 24 February 2026).
55. Abdulhaq, H. *Earth Engine Hydroclimate Dashboard (Streamlit)*; Zenodo: Geneva, Switzerland, 2025; Available online: https://zenodo.org/doi/10.5281/zenodo.17912092 (accessed on 17 December 2025). [CrossRef]
56. Mann, M.E. On Smoothing Potentially Non-Stationary Climate Time Series. *Geophys. Res. Lett.* **2004**, *31*, L07214. [CrossRef]
57. Arguez, A.; Vose, R.S. The Definition of the Standard WMO Climate Normal: The Key to Deriving Alternative Climate Normals. *Bull. Am. Meteorol. Soc.* **2011**, *92*, 699–704. [CrossRef]
58. Guilbert, J.; Betts, A.K.; Rizzo, D.M.; Beckage, B.; Bomblies, A. Characterization of Increased Persistence and Intensity of Precipitation in the Northeastern United States. *Geophys. Res. Lett.* **2015**, *42*, 1888–1893. [CrossRef]
59. Zhang, X.; Alexander, L.; Hegerl, G.C.; Jones, P.D.; Klein Tank, A.M.G.; Peterson, T.C.; Trewin, B.; Zwiers, F.W. Indices for Monitoring Changes in Extremes Based on Daily Temperature and Precipitation Data. *WIREs Clim. Change* **2011**, *2*, 851–870. [CrossRef]
60. Alexander, L.V.; Zhang, X.; Peterson, T.C.; Caesar, J.; Gleason, B.; Klein Tank, A.M.G.; Haylock, M.; Collins, D.; Trewin, B.; Rahimzadeh, F.; et al. Global Observed Changes in Daily Climate Extremes of Temperature and Precipitation. *J. Geophys. Res. Atmospheres* **2006**, *111*, D05109. [CrossRef]
61. Zhang, X.; Yang, F. *RClimDex (0.9) User Manual*; Climate Research Branch Environment Canada: Toronto, ON, Canada, 2004.
62. Tomczyk, A.M.; Szyga-Pluta, K. Variability of Thermal and Precipitation Conditions in the Growing Season in Poland in the Years 1966–2015. *Theor. Appl. Climatol.* **2019**, *135*, 1517–1530. [CrossRef]
63. Alduchov, O.A.; Eskridge, R.E. Improved Magnus Form Approximation of Saturation Vapor Pressure. *J. Appl. Meteorol.* **1996**, *35*, 601–609. [CrossRef]
64. Lawrence, M.G. The Relationship between Relative Humidity and the Dewpoint Temperature in Moist Air: A Simple Conversion and Applications. *Bull. Am. Meteorol. Soc.* **2005**, *86*, 225–233. [CrossRef]
65. Abdulhaq, H. *Geoscience & Data Visualization Python Toolkit (Streamlit, Mapping, Interpolation, and Stats)*; Zenodo: Geneva, Switzerland, 2025.
66. Importing Table Data (Shapefile/CSV). In *Google Earth Engine Developers Guide*; Google Earth Engine: Mountain View, CA, USA, 2022; Available online: https://developers.google.com/earth-engine/guides/table_upload (accessed on 24 February 2026).
67. Manage Assets. In *Google Earth Engine Developers Guide*; Google Earth Engine: Mountain View, CA, USA, 2024; Available online: https://developers.google.com/earth-engine/guides/manage_assets (accessed on 24 February 2026).
68. Earth Engine Code Editor. In *Google Earth Engine Developers Guide*; Google Earth Engine: Mountain View, CA, USA, 2024; Available online: https://developers.google.com/earth-engine/guides/playground (accessed on 24 February 2026).
69. Leung, T.I. Best Practices for Using AI Tools as an Author, Peer Reviewer, or Editor. *J. Med. Internet Res.* **2023**, *25*, e51584. [CrossRef]
70. World Association of Medical Editors (WAME). *Chatbots, Generative AI, and Scholarly Manuscripts: WAME Recommendations on Chatbots and Generative Artificial Intelligence in Relation to Scholarly Publications*; World Association of Medical Editors (WAME): Milan, Italy, 2023.
71. International Committee of Medical Journal Editors (ICMJE). *Up-Dated ICMJE Recommendations (January 2024)*; International Committee of Medical Journal Editors (ICMJE): Vancouver, BC, Canada, 2024.
72. GitHub Docs. GitHub Copilot Documentation. Available online: https://docs.github.com/en/copilot (accessed on 24 February 2026).
73. Abdulhaq, H. Predicting Thermal Performance of Aquifer Thermal Energy Storage Systems in Depleted Clastic Hydrocarbon Reservoir via Machine Learning: Case Study from Hungary. In Proceedings of the 16th European Geothermal PhD Days Book of Abstracts (EGPD 2025), Szeged, Hungary, 8–11 April 2025.
74. Abdulhaq, H.A.; Geiger, J.; Vass, I.; Tóth, T.M.; Bozsó, G.; Szanyi, J. A Data-Driven ML Model for Sand Channel Prediction from Well Logs for UTES Site Optimization and Thermal Breakthrough Prevention: Hungary Case Study. *Energies* **2025**, *18*, 4230. [CrossRef]
75. Djrust26. Aszály a Nyírségben—Már az év Eleje is Csapadékmentesen Indult 2022-ben. Available online: https://www.nyiregyhaza.hu/post/aszaly-a-nyirsegben-mar-az-ev-eleje-is-csapadekmentesen-indult-2022-ben-2022-05-25 (accessed on 30 December 2025).
76. MNO. A Talajvíz Szintje Megdöntötte az 1936-os Rekordot is + Képriport. Available online: https://magyarnemzet.hu/archivum-archivum/2010/12/a-talajviz-szintje-megdontotte-az-1936-os-rekordot-is-kepriport (accessed on 30 December 2025).

77. Feng, C.; Wang, H.; Lu, N.; Chen, T.; He, H.; Lu, Y.; Tu, X.M. Log-Transformation and Its Implications for Data Analysis. *Shanghai Arch. Psychiatry* **2014**, *26*, 105–109. [CrossRef]
78. Simon, S.; Déri-Takács, J.; Szijártó, M.; Szél, L.; Mádl-Szőnyi, J. Wetland Management in Recharge Regions of Regional Groundwater Flow Systems with Water Shortage, Nyírség Region, Hungary. *Water* **2023**, *15*, 3589, Correction in *Water* **2024**, *16*, 1609. https://doi.org/10.3390/w16111609. [CrossRef]
79. Belügyminisztérium Magyarország. *Évi Vízgyűjtő-Gazdálkodási Terve: "A Duna-Vízgyűjtő Magyarországi Része Vízgyűjtő-Gazdálkodási Terv—2021" Dokumentumának Összefoglaló Rövidített Változata*; Belügyminisztérium: Budapest, Hungary, 2022.
80. Czomba, P.; Vass, R.; Túri, Z. Statistical Analysis of the Hydrological and Hydrometeorological Characteristics of the Upper Tisza Basin. *J. Environ. Geogr.* **2023**, *16*, 133–139. [CrossRef]
81. *NDVI, the Foundation for Remote Sensing Phenology*; U.S. Geological Survey; Reston, VA, USA, 2018. Available online: https://www.usgs.gov/special-topics/remote-sensing-phenology/science/ndvi-foundation-remote-sensing-phenology (accessed on 10 February 2026).
82. Varlas, G.; Papadaki, C.; Stefanidis, K.; Mentzafou, A.; Pechlivanidis, I.; Papadopoulos, A.; Dimitriou, E. Increasing Trends in Discharge Maxima of a Mediterranean River during Early Autumn. *Water* **2023**, *15*, 1022. [CrossRef]
83. Unnisa, Z.; Govind, A.; Lasserre, B.; Marchetti, M. Water Balance Trends along Climatic Variations in the Mediterranean Basin over the Past Decades. *Water* **2023**, *15*, 1889.
84. Pérez-Palazón, M.J.; Pimentel, R.; Polo, M.J. Climate Trends Impact on the Snowfall Regime in Mediterranean Mountain Areas: Future Scenario Assessment in Sierra Nevada (Spain). *Water* **2018**, *10*, 720. [CrossRef]
85. Kovács, A.; Ilyés, C.; Mohammed, M.A.A.; Szűcs, P. Assessing Climate Change Impacts on Spring Discharge in Data-Sparse Environments Using a Combined Statistical–Analytical Method: An Example from the Aggtelek Karst Area, Hungary. *Water* **2025**, *17*, 2507. [CrossRef]
86. Bartholy, J.; Pongrácz, R.; Pieczka, I. How the Climate Will Change in This Century? *Hung. Geogr. Bull.* **2014**, *63*, 55–67. [CrossRef]
87. ClimateChangePost. Climate Change. Available online: https://www.climatechangepost.com/countries/hungary/climate-change/ (accessed on 16 January 2026).
88. Kis, A.; Pongrácz, R. Future Changes of Snow-Related Variables in Different European Regions. *Hung. Geogr. Bull.* **2023**, *72*, 3–22. [CrossRef]
89. Hungary Climate Resilience Policy Indicator—Analysis. Available online: https://www.iea.org/articles/hungary-climate-resilience-policy-indicator (accessed on 16 January 2026).
90. Rybchynska, V.; Pysarenko, L.; Pushkar, H.; Savenets, M.; Osadchyi, V. Seasonal Changes in Evaporation and Potential Evapotranspiration under Different Scenarios of Climate Change on the Territory of Ukraine. In Proceedings of the European Geosciences Union General Assembly 2025 (EGU25), Vienna, Austria, 27 April–2 May 2025.
91. Kumar, R.; Samaniego, L.; Thober, S.; Rakovec, O.; Marx, A.; Wanders, N.; Pan, M.; Hesse, F.; Attinger, S. Multi-Model Assessment of Groundwater Recharge Across Europe Under Warming Climate. *Earths Future* **2025**, *13*, e2024EF005020. [CrossRef]
92. Kovács, A.; Jakab, G. Modelling the Impacts of Climate Change on Shallow Groundwater Conditions in Hungary. *Water* **2021**, *13*, 668. [CrossRef]
93. Zheng, Y.; Ross, A.; Villholth, K.G.; Dillon, P. (Eds.) *Managing Aquifer Recharge: A Showcase for Resilience and Sustainability*; UNESCO: Paris, France, 2021.
94. Bouwer, H. Artificial Recharge of Groundwater: Hydrogeology and Engineering. *Hydrogeol. J.* **2002**, *10*, 121–142. [CrossRef]
95. Laraichi, S.; Hammani, A.; Bouignane, A. Data Integration as the Key to Building a Decision Support System for Groundwater Management: Case of Saiss Aquifers, Morocco. *Groundw. Sustain. Dev.* **2016**, *2–3*, 7–15. [CrossRef]
96. Pierce, S.A.; Sharp, J.M.J.; Eaton, D.J. Decision Support Systems and Processes for Groundwater. In *Integrated Groundwater Management: Concepts, Approaches and Challenges*; Springer: Cham, Switzerland, 2016; pp. 639–665.
97. Fitch, P.; Brodaric, B.; Stenson, M.; Booth, N. Integrated Groundwater Data Management. In *Integrated Groundwater Management: Concepts, Approaches and Challenges*; Springer: Cham, Switzerland, 2016; pp. 667–692.
98. Abdulhaq, H.A.; Geiger, J.; Vass, I.; Tóth, T.M.; Medgyes, T.; Szanyi, J. Transforming Abandoned Hydrocarbon Fields into Heat Storage Solutions: A Hungarian Case Study Using Enhanced Multi-Criteria Decision Analysis–Analytic Hierarchy Process and Geostatistical Methods. *Energies* **2024**, *17*, 3954. [CrossRef]
99. Lechner Knowledge Center. Agricultural Water Use Information and Control Framework System (VIZEK). Available online: https://lechnerkozpont.hu/en/oldal/agricultural-water-use-information-and-control-framework-system-vizek (accessed on 24 February 2026).
100. Országos Vízügyi Főigazgatóság (OVF). *Vízhasználat Információs, Ellenőrzési És Integrált Hatósági Feladatokat Ellátó Keretrendszer (VIZEK) Kialakítása*; Országos Vízügyi Főigazgatóság (OVF): Budapest, Hungary, 2023.
101. Morlot, M.; Rigon, R.; Formetta, G. Hydrological Digital Twin Model of a Large Anthropized Italian Alpine Catchment: The Adige River Basin. *J. Hydrol.* **2024**, *629*, 130587. [CrossRef]
102. Thomann, J.A.; Werner, A.D.; Irvine, D.J. Developing Adaptive Management Guidance for Groundwater Planning and Development. *J. Environ. Manag.* **2022**, *322*, 116052. [CrossRef]

103. Allen, R.G.; Pereira, L.S.; Raes, D.; Smith, M. *Crop Evapotranspiration: Guidelines for Computing Crop Water Requirements*; FAO Irrigation and Drainage Paper; Food and Agriculture Organization of the United Nations (FAO): Rome, Italy, 1998.
104. Feng, G.; Jin, W.; Ouyang, Y.; Huang, Y. The Role of Changing Land Use and Irrigation Scheduling in Groundwater Depletion Mitigation in a Humid Region. *Agric. Water Manag.* **2024**, *291*, 108606. [CrossRef]